Shaping bridge decks for VIV mitigation: A wind tunnel data-driven adaptive surrogate-based optimization method

Miguel Cid Montoya[a], Hua Bai[b,*], Mao Ye[b]

[a]*ASTRO Lab, Department of Engineering, Texas A&M University-Corpus Christi, Corpus Christi, TX 78412, USA*
[b]*Research Center of Highway Large Structure Engineering on Safety, School of Highway, Chang'an University, Xi'an, 710064, Shaanxi, China*

Abstract

Vortex-induced vibration (VIV) of deck girders frequently drives the wind-resistant design of wind-sensitive bridges from the preliminary to final design stages. Shaping bridge decks is a proven strategy to mitigate VIV. While significant shape modifications are commonly restricted to preliminary design stages, only minor medications are possible at advanced design stages, typically involving adding flow modifiers or changing the shape and location of existing appendages. These mitigation strategies have been implemented in the last decades by carrying out expensive wind tunnel campaigns and following heuristic design rules. This paper proposes an experimental data-driven adaptive surrogate-based optimization approach to systematically identify optimum deck shapes that minimizes the economic cost of the bridge while fulfilling the VIV project specifications. The methodology is conceived to carry out simultaneously the general and detailed shape design of the final deck configuration by harnessing a sequential sampling plan aiming at reducing the sectional model construction costs. The proposed holistic design framework is successfully applied to a real application case involving 26 wind tunnel tests of 1.8-meter wide sectional models to figure out the optimal gap distance and location of maintenance tracks of a twin-box deck equipped with all the appendages included in the final deck design.

Keywords: Vortex-induced vibrations, wind tunnel testing, long-span bridges, surrogate models, aerodynamic optimization, data-driven design, construction costs

1. Introduction

Contemporary cable-supported bridges are often built with trapezoidal single- and multi-box girders, given their remarkable mechanical and aeroelastic contribution to the bridge's performance. However, long-span bridges equipped with these effective deck cross-section geometries are susceptible to vortex-induced vibrations (VIV) in both construction and completed phases of the bridge life cycle. In fact, VIV and flutter instability are the two aeroelastic phenomena that

*Corresponding author
Email addresses: miguel.cidmontoya@tamucc.edu (Miguel Cid Montoya), baihua15@chd.edu.cn (Hua Bai), 2021121065@chd.edu.cn (Mao Ye)

more often have conditioned the design of the longest long-span bridges worldwide (Ge [1]). Very well-known cases of VIV in long-span bridges include the Tacoma Narrows Bridge during its 4-month service life (Larsen and Larose [2]), the Great Belt suspension bridge (Larsen et al. [3]), the Messina Bridge project (Diana et al. [4]), and the Xihoumen Bridge (Zhang et al. [5], Yang et al. [6]), among many others. A comprehensive list of bridges that experienced VIV can be found in Xu et al. [7]. VIV can be particularly dangerous during some construction phases before reaching the final bridge configuration. An interesting case was the Alconétar Bridge in Spain (Astiz [8]), where vertical oscillations were recorded under winds as low as 5.5 m/s. Recent cases were also reported in contemporary constructions, such as the Humen Pearl River Bridge in Guangdong, China, which was temporarily closed due to VIV in May 2020 (Ge et al. [9]).

Twin-box decks are an attractive deck typology for long-span bridges due to their outstanding aeroelastic performance that permits increasing the bridge critical wind velocity (Zasso et al. [10]) and their remarkable lateral stiffness contribution (Argentini et al. [11]). The aeroelastic benefits of twin-box decks and the impact of the gap distance between boxes on the aerodynamics and self-excited forces were the objects of several research studies, such as those reported by Qin et al. [12], Kwok et al. [13], Yang et al. [14, 15], Trein et al. [16], Nieto et al. [17]. The impact of the gap distance and box shape in the admittance functions of a twin-box deck was investigated by Wang et al. [18, 19]. On the other hand, the susceptibility of twin-box decks to VIV due to the formation of vortices in the gap between boxes has been another hot research topic in bridge engineering, particularly in the last decade. Laima and Li. [20] defined three different flow patterns depending on the gap-to-depth ratio G/D for the girder cross-section of the Xihoumen Bridge by using wind tunnel tests. The gap-to-depth ratios that define the change of flow pattern were identified to be $C/D = 2.138$ from the first to the second pattern and $C/D = 10.26$ from the second one to the third pattern. The numerical investigation by Álvarez et al. [21] confirmed the existence of a critical gap-to-depth ratio between the two flow patterns for the boxes of the Stonecutters Bridge, this time at $C/D = 2.35$. In the first pattern, typically identified as short gap arrangements, vortices are not fully developed in the central slot, which prevents the leeward box from being immersed in the wake of the windward box, as is the case of the second pattern. This is a key feature to consider in the wind-resistant design of twin-box decks.

VIV causes undesired displacements and accelerations along the deck that must be mitigated according to the guidelines of construction codes (ASCE Committee on Cable-Stayed Bridges [22], JTGT 3360-01-2018 [23], ISO 2631 [24]) and project specifications (Stretto di Messina [25]) to keep the desired serviceability standards and resistance against fatigue (Hosomi et al. [26]). These undesired effects are typically addressed by introducing inertial modifications (Ge et al. [9], Gu et al. [27], Battista and Pfeil [28]) or tailoring the deck shape (Brown [29], Larsen and Wall [30], Belloli et al. [31]). The deck shape can be modified by changing the cross-section

geometry in preliminary design stages (Argentini et al. [11]) or later in the final or detailed design phase. Alternatively, retrofitting interventions can be carried out when needed (Vejrum et al. [32], Barelli et al. [33]), typically involving appendages such as guide vanes to mitigate undesired VIV (Larsen et al. [3], Kargarmoakhar et al. [34]). Larsen and Wall [30] discussed the economic benefits of adopting effective deck shapes from the preliminary stages of the bridge design instead of mitigating undesirable aeroelastic responses by a posteriori expensive interventions. As explained in this reference, "While the guide vanes constitute an efficient way of mitigating vortex-induced oscillations of box girder decks, they also present an increase of maintenance efforts and construction costs." ... "Hence it is desirable to be able to design a trapezoidal box section which does not display vortex shedding excitation and thus avoid appendages." The benefits of adopting mitigation strategies during the design stage to later avoid the need to install flow modifiers to palliate undesired wind-induced responses are apparent.

The first experimental studies considering the influence of the shape on the VIV response were reported by Nakamura and Mizota [35], Komatsu and Kobayashi [36], Shiraishi and Matsumoto [37], among many others. The shape of the fairing angle and the presence of countermeasures have an important impact on the VIV response (Bai et al. [38]). The impact of the location of guide vanes on the VIV response was studied by Li et al. [39]. Alternative mitigation approaches can also involve adding grid plates on the gap between the boxes to control the VIV and flutter responses, as investigated by Zhou et al. [40]. The location and shape of appendages also affect other aeroelastic responses, such as flutter, as studied in Yang et al. [41] for the flutter response of a twin-box deck. Another alternative to mitigate VIV is tailoring the traffic barriers, as proposed by Bai et al. [42]. A comprehensive review of existing techniques to mitigate VIV on bridge decks was recently published by Gao et al. [43]. Moreover, interesting investigations about VIV mitigation in triple-box girders can be found in Belloli et al. [31], Wang et al. [44].

Handling deck shape variables such as the gap distance and the location of unavoidable appendages such as maintenance rails is a prevalent design issue in bridge engineering practice. A clear example is the deck configuration of the Çanakkale Bridge (Güzel [45]), Türkiye, completed in 2022 and currently holds the longest main span world record with an outstanding length of 2023 m. Figure 1 shows the bottom side of the deck, where it can be seen that the gap distance and the location of the maintenance rails drive the aerodynamic design. These design challenges are typically addressed in the industry by independent wind tunnel studies, sometimes in a sequential process that can even be carried out by different consultants or laboratories. This procedure prevents designers from fully exploring all possible design alternatives, i.e., effectively inspecting the entire shape design space by dealing with all relevant shape design variables simultaneously. In the present study, we propose an alternative holistic design strategy that simultaneously addresses all shape design variables to identify the optimum deck configuration.

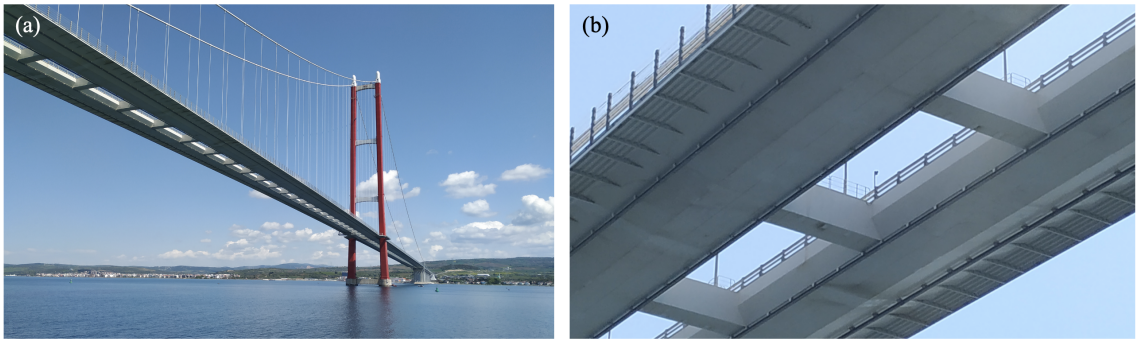

Figure 1: Pictures of the 1918 Çanakkale Bridge, Türkiye: (a) General view of the bridge from the Dardanelles; and (b) detail of the bottom side of the deck with the maintenance rails.

On the other hand, either in industrial projects or in research studies, the selection of the most effective countermeasures and required appendages, their shape and location, the boxes' shape, and other relevant design variables are commonly based on the engineer's experience or intuition, namely "heuristics," and trial-error processes. While heuristics are fundamental to addressing complex bridge design challenges (Arıoğlu [46]), numerical design methods are a powerful alternative to improve heuristic-based designs further. Moreover, once the most effective appendages are selected, other design variables involving their shape and location are typically studied nowadays using mathematical combinatorics, hence performing an ineffective shape design exploration. These approaches can be advanced by adopting contemporary data-driven optimization methods.

Data-driven optimization approaches were conceived as early as 1965 by Schmit and Thornton [47], where a first attempt was made to optimize a double-wedge supersonic wing by minimizing a combination of the structural weight and aerodynamic drag. Later developments advanced this approach, defined and formulated in Vanderplaats [48] as "experimental optimization" by extracting aerodynamic data from approximation functions. Later developments by Hansen and Vanderplaats [49] led to the origins of surrogate-based optimization. Emulation methods such as surrogate modeling (Forrester and Keane [50], Queipo et al. [51], Yondo et al. [52]) and machine learning (Adeli and Hung [53], Rizzo and Caracoglia [54]), and even their combination (Erten et al. [55]), are promising alternatives to enable the implementation of optimization algorithms in the wind-resistant design of bridges. Some applications based on CFD simulations have recently been published (Nieto et al. [17], Cid Montoya et al. [56], Xu et al. [57]). However, despite the recent advances in CFD-based aero-structural optimization methods (Cid Montoya et al. [58, 59], Cid Montoya [60]), and its application to twin-box decks considering bare sections (Cid Montoya et al. [61, 62]), more research is needed to properly carry out the deck optimization considering the critical role of appendages in VIV responses. Alternatively, surrogate models can be trained using high-fidelity experimental data. Wind tunnel testing is a very effective design tool (Diana et al. [63]), particularly when studying complex geometries including barriers and appendages whose shape and porosity effects (Buljac et al. [64]) can not be adequately mod-

eled using CFD simulations. For instance, Li et al. [65] quantified the aerodynamic forces on truss girders using wind tunnel tests, given the limitations of CFD simulations to accurately model those complex geometries with multiple isolated elements. Similarly, aeroelastic responses, such as VIV, can be emulated using wind tunnel data. Hence, the fusion of numerical design techniques with wind tunnel testing stands as a ready-to-use alternative that can efficiently search for optimal design considering the most relevant design constraints of the problem while guaranteeing an accurate reproduction of any complex aerodynamic feature.

Hence, this paper proposes the fusion of wind tunnel testing techniques and surrogate-based optimization strategies to develop an efficient data-driven surrogate-based design optimization methodology. This results in a synergistic strategy that takes advantage of the benefits of each approach. On the one hand, the accuracy of wind tunnel testing permits the creation of a high-fidelity emulator to achieve a reliable, optimum design. On the other hand, adopting data-driven surrogate-based optimization methods guarantees efficient design space exploration to achieve the optimum combination of all the design variables while balancing all economic and aeroelastic performance goals and requirements. The proposed data-driven approach is conceptually introduced in Section 2, where the conceptual formulation of the optimization problem is posed in Section 2.1 and the selection of the sampling plan aiming at reducing the sectional models' construction costs is discussed. The real twin-box deck girder adopted as an application example is presented in Section 3. The shape design variables were selected to cover a wide range of possible maintenance rails locations and gap-to-depth ratios ($C/D = [0.714, 3.571]$). This range of gap-to-depth ratios includes the two relevant patterns identified in Laima and Li. [20], hence, allowing the optimization algorithm to identify the optimum design within a meaningful shape design domain that includes gap-to-depth ratios similar to those of relevant real bridges, such as the Yi Sun-sin Bridge ($C/D = 1.56$, main span 1545 m), the Xihoumen Bridge ($C/D = 1.71$, main span 1650 m), the Çanakkale Bridge ($C/D = 2.57$ (Güzel [45]), main span 2023 m), and the Stonecutters Bridge ($C/D = 4$ (slightly higher), main span 1018 m). Section 3.1 describes the wind tunnel tests carried out to obtain the VIV responses. The specific optimization problem for this application case is formulated in Section 3.4, where the constrained optimization problem is posed to effectively handle the bimodal VIV responses. Section 4 describes the evolution of the surrogate-based optimization process and the wind tunnel data obtained for every design tested in the context of this investigation. The reported experimental database is a valuable reference for the VIV-resistant design of twin-box decks equipped with maintenance rails. The achievements of the VIV-mitigation optimization strategy used in this study are discussed in Section 4.7, where the initial and optimum designs are compared. Finally, Section 5 reports some concluding remarks.

2. Data-driven adaptive surrogate-based optimization methodology

The methodology proposed in this study is a fusion of surrogate-based optimization methods with wind tunnel testing to find optimum designs with minimum economic cost while mitigating undesired VIV response following the specifications of construction codes. To achieve this goal, it is fundamental to adopt holistic design strategies that consider all relevant design variables and constraints simultaneously in the design optimization problem. The key feature of the strategy described in Figure 2 to deal with the dimensionality issues associated with holistic design approaches is the outer loop. It permits moving from a global exploration in the first cycle, aiming at moving closer to the optimum design, to subsequent iterations that update the surrogate model by performing local samplings in the neighborhood of the solution. This methodology permits converging to the optimum design with a contained number of wind tunnel tests in the first cycle while guaranteeing the accuracy of the surrogate in the vicinity of the optimum design thanks to the surrogate updates trained with the local samplings.

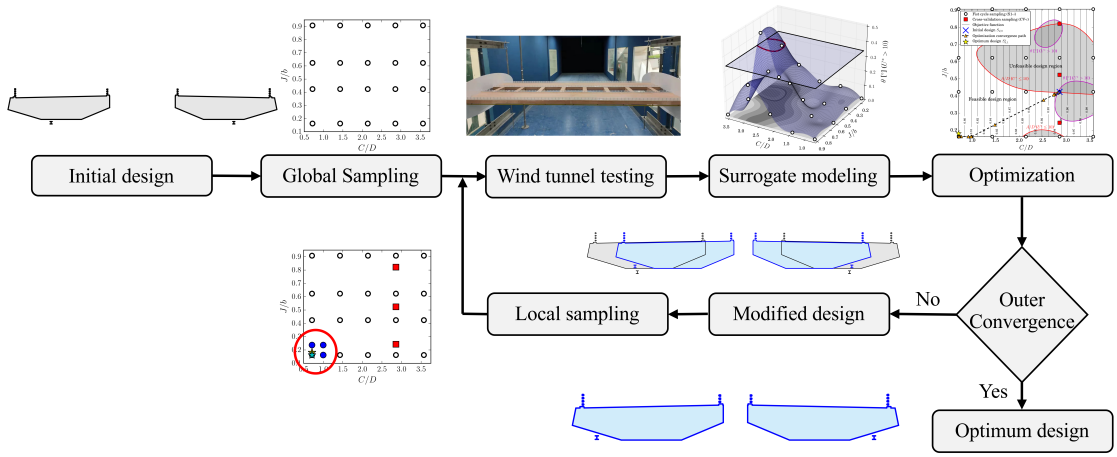

Figure 2: Flowchart of the proposed data-driven surrogate-based optimization methodology.

The main phases of the procedure are described in Figure 2. The first phase involves selecting the initial design and a complete set of design variables and their allowed modifications, i.e., the definition of the shape design space. In the following step, a global sampling plan is carried out to identify the candidate designs that must be tested in the entire design domain to produce the required data to build the surrogate model. As discussed in Section 2.3, a full factorial stratification strategy is used given its advantages of carrying out multiple wind tunnel tests following an efficient pattern, which permits reducing the construction cost of sectional models. After obtaining the results of the sectional model wind tunnel test for the designs prescribed in the sampling plan, a global surrogate model will be built and trained with the experimental data, as described in Section 2.2. This surrogate, along with the economic model specifically defined for each application case, will be used in the design optimization. Some insights about the surrogate-based optimization techniques are provided in Section 2.1, along with the formulation proposed for the

optimization process. An outer convergence check is carried out after the surrogate-based optimization, which decides if a new cycle is required or not. In the new cycle, the optimum design previously obtained is adopted as the current design, and a new local sampling is carried out in the neighborhoods of this design following an active learning strategy. Then, new wind tunnel tests are carried out to update the surrogate focusing on the region of interest, and the optimization is repeated to update the design with the highest level of accuracy. This procedure seeks to avoid any undesired VIV effect that can be found between samples due to the high nonlinear nature of bridge aerodynamics.

2.1. Surrogate-based optimization formulation

The deck shape design problem is formulated herein as an optimization problem that seeks to minimize the deck construction costs while fulfilling the VIV acceptance criteria. Given that the VIV performance is evaluated based on thresholds imposed by construction codes and standards, it must be formulated as a set of design constraints. On the other hand, the objective function to minimize will be the bridge cost. Hence, the constrained optimization problem is formulated as follows:

$$
\begin{aligned}
&\text{find}: \ \mathbf{S}_d = (S_k), \qquad k = 1, ..., N \\
&\text{minimize}: F(\mathbf{S}_d) \\
&\text{subject to}: \\
&\quad g_v^{VIV}(\mathbf{x}_s) = \frac{R_v}{R_{v,max}} - 1 \leq 0, \qquad v = 1, ..., V_n \\
&\quad S_k^L \leq S_k \leq S_k^U, \qquad k = 1, ..., N,
\end{aligned}
\tag{1}
$$

where $\mathbf{S}_d$ is the complete set of design variables, including the shape and dimensions of the boxes and the shape and location of appendages and barriers, among others. The value of the objective function F, which is a function of the deck shape $\mathbf{S}_d$, is given by the economic model, as described in Section 3.5. The constrained optimization problem includes each v behavior constraint related to the VIV response g_v^{VIV} for all degrees of freedom and angles of attack considered in the design. Moreover, lateral constraints limit the possible values of each design variable S_k. The VIV response R_v is limited by a threshold $R_{v,max}$ given by construction codes and project specifications. The VIV responses are provided by the VIV emulator trained with wind tunnel test results, turning this design problem into a surrogate-based constrained design optimization problem. Alternative formulations to deal with these two conflicting criteria were proposed by Putil et al. [66]. Section 3 describes the specific variables and values adopted in the problem solved in this study.

2.2. VIV surrogate-enabled emulation

Kriging emulator $\hat{f}_K$ (Krige [67], Sacks et al. [68]) is a very efficient alternative in problems with scarce and costly samples, given its ability to reproduce the exact value of all samples used in the training process. The model is made of a regression model or trend function $\boldsymbol{\kappa}(\boldsymbol{x})^T\boldsymbol{\rho}$ and a stationary Gaussian process error model $\varepsilon(\boldsymbol{x})$ that corrects the trend function:

$$\hat{f}_K(\boldsymbol{x}) = \boldsymbol{\kappa}(\boldsymbol{x})^T\boldsymbol{\rho} + \varepsilon(\boldsymbol{x}). \tag{2}$$

The most used regression models are zero, first, and second-order polynomials. The stationary Gaussian process has zero mean, constant variance, and a stationary autocorrelation function $r(\boldsymbol{x}, \boldsymbol{x'})$. The anisotropic generalized exponential model is used as autocorrelation function $r(\boldsymbol{x}, \boldsymbol{x'})$, which can be written as:

$$r(\boldsymbol{x}, \boldsymbol{x'}) = exp\left(-\sum_{k=1}^{D}\theta_k\left|x_k - x_k{}'\right|^{\gamma}\right), \tag{3}$$

where D is the number of input dimensions, θ_k are the correlation parameters, and γ is a parameter in the range $[0, 2]$ (Forrester et al. [69]).

The surrogate model used in this study is trained with the VIV experimental data obtained from the wind tunnel with the goal of emulating the VIV response for any set of shape design variables $\boldsymbol{S}_d$. Hence, the VIV surrogate model $\mathcal{V}$ is a high-fidelity model that can be written using a black-box perspective as follows:

$$\mathcal{V}(\boldsymbol{S}_d) = \left[A/D\left(U^* \leq U^*_{\text{cut-off}}\right), A/D\left(U^*_{\text{cut-off}} < U^*\right), \theta\left(U^* \leq U^*_{\text{cut-off}}\right), \theta\left(U^*_{\text{cut-off}} < U^*\right)\right], \tag{4}$$

where A stands for the vertical amplitude, which is expressed as a non-dimensional value by dividing it by the deck depth D, θ is the rotational response, and U^* is the reduced velocity. A cut-off reduced velocity $U^*_{\text{cut-off}}$ is adopted in order to treat each peak of the bimodal VIV response individually in the optimization problem. This permits the gradient-based optimization algorithm to catch the sensitivity of the changes in the design variables to the VIV responses. If the VIV response shows a multi-modal behavior, several cut-off reduced velocities can be used.

2.3. Design space exploration: sampling plan

A fundamental step in emulation-based strategies is the methodology adopted for selecting the samples used to train the surrogate model, i.e., the sampling plan. There are multiple sampling techniques (Sacks et al. [68], McKay et al. [70], Olsson et al. [71], Picheny et al. [72]), with specific advantages and drawbacks. Fundamental concepts about sampling strategies can be found in Forrester et al. [69], Montgomery [73], and a comprehensive review in Yondo et al. [52]. The

selection of the most adequate design technique for each kind of problem is an open issue that must be carefully considered. It is especially important in design problems where the analysis of the samples involves a high economic cost, as is the case of experimental data-driven surrogates. In computational environments, the cost of the sampling plan is typically only dependent on the number of samples, and the specific designs adopted for each sample do not impact the evaluation cost. This is commonly the case with CFD-based design methodologies and permits adopting any sampling plan that maximizes the design exploration performance. However, the evaluation costs in experimental studies can be drastically conditioned by the designs included in the sampling plan. Remarkably, in sectional model wind tunnel testing, the repetition of specific values of design variables can drastically reduce the sectional model construction costs and workload since some parts of the model can be reused for new samples. For instance, the boxes of a twin-box deck can be reused when studying the impact of the gap distance on the VIV performance. For this reason, factorial stratification techniques (Montgomery [73]) are very competitive in experimental environments, as it will be further discussed in Section 4.1. Moreover, full factorial techniques permit the accurate calculation of sensitivities of the response with regard to the design variables without relying on estimations from the surrogate model. Finally, it must be highlighted that the iterative nature of the procedure described in Figure 2 guarantees the accurate design space exploration in the neighborhoods of the optimum design independently of the sampling strategy adopted.

3. Description of the application case

The performance of the methodology described above is tested herein by adopting a twin-box cable-stayed bridge with a 720-meter main span as the application example. The gap distance between the girder boxes and the position of the repair and maintenance tracks are the design modifications considered to mitigate the VIV responses. Therefore, two shape design variables $\mathbf{S}_d$ are adopted in the optimization problem as depicted in blue in Figure 3: (1) the gap distance C; and (2) the bridge overhaul vehicle track position J. Hence, $\boldsymbol{S}_d = [C, J]$. The initial design has a gap distance of $C_0 = 11.2$ m, which results in a total width of the deck $B_0 = 45.84$ m. J is defined as the horizontal distance from the outer corner of the box to the position of the track. The initial design of the shape design variables S_0 along with their lower bound S^L and upper bounds S^U, as formulated in Equation (1), are reported in Table 1. They are also expressed as non-dimensional quantities as C/D and J/b, respectively, where D stands for the deck depth and b is the width of each individual box. These two parameters are kept constant along the design optimization process, taking the values of $D = 3.92$ m and $b = 17.32$ m, both in full scale. The gap-to-depth ratio C/D ranges from 0.714 to 3.571, according to the limit values permitted to the gap distance C (see Table 1). The initial design has a gap-to-depth ratio of $C/D = 2.857$. The chosen gap-to-depth

ratio range represents feasible values currently used for bridges built worldwide and covers the first two flow patterns identified by Laima and Li. [20]. The Yi Sun-sin Bridge and the Xihoumen Bridge can be classified into the first flow pattern, with gap-to-depth ratios of 1.56 and 1.71, respectively, below the critical value of 2.138 identified by Laima and Li. [20]. The Çanakkale Bridge has a gap-to-depth ratio of 2.57, which is very close to the initial design adopted in the present study and above the critical value. It must be noted that the critical value that identifies the flow structure change is affected by the specific appendages (e.g., maintenance rails) and the cross-section of the boxes (e.g., gap geometry) of each bridge deck, which turns this classification into case-specific. The Stonecutters Bridge is another example of a larger gap reaching a value of about 4, which is close to the upper bound of the design domain considered in the present study.

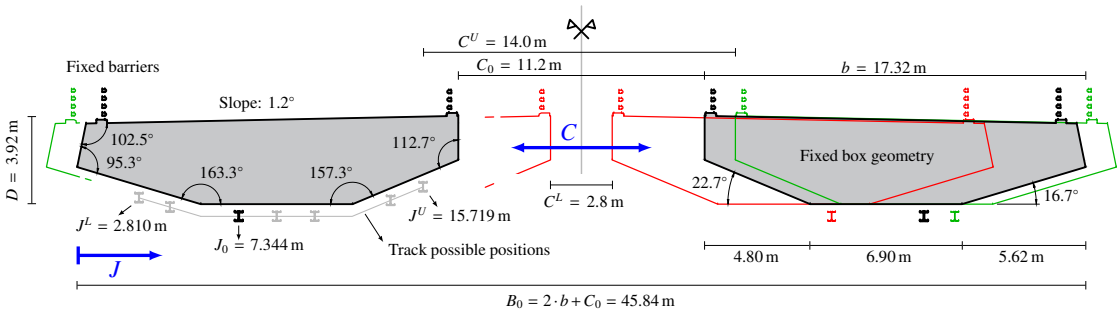

Figure 3: Deck cross-section geometry of the initial design (in gray) and possible deck shape modifications controlled by design variables C and J (in blue). The configuration with maximum C^U and minimum C^L gap distance are shown in green and red, respectively. The possible positions for the bridge overhaul vehicle track are shown in gray on the left box, which ranges from the minimum J^L to the maximum J^U distance measured from the deck outer corner to the track position. Dimensions in m in full scale.

Table 1: List of shape design variables $\mathbf{S}_d$ considered in the optimization problem, including the values of the initial design $S_{k,0}$, lower bound S_k^L and upper bound S_k^U.

Design variable	Description	Scale	S_0	S^L	S^U
C	Gap distance	Full [m]	11.200	2.800	14.000
		Reduced [mm]	160.0	40.0	200.0
		Normalized (C/D)	2.857	0.714	3.571
J	Track position	Full [m]	7.344	2.810	15.719
		Reduced [mm]	104.9	40.1	224.6
		Normalized (J/b)	0.424	0.162	0.908

3.1. Wind tunnel tests

The wind tunnel tests were conducted in the CA-1 Wind Tunnel Laboratory of Chang'an University. The CA-1 wind tunnel is a closed-circuit wind tunnel with a turbulence intensity below 0.3%. The test section is 3.0 m wide and 2.5 m high. The test wind speed can be adjusted

continuously from 1.5 m/s to 15 m/s, and the step length is 0.2 m/s. The wind speed ratio is 1:4. The sectional model is 1.8 m long and 0.72 m wide. The scale of the model is 1:70. The model is made of light wood, with an aluminum alloy frame and two end plates made of extruded plate material at both ends to eliminate the influence of flow around the end, as shown in Figure 4. The bridge depth is kept constant, adopting a dimension of 3.92 m at full scale and 56 mm at the wind tunnel scale. The blockage ratio of the wind tunnel test model is 1.4%. The gap distance is one of the design variables of the problem, and the total width is a function of the gap $B = 2 \cdot b + C$. All appendages, including the bridge overhaul vehicle track and barriers, are built in detail for each sectional model, as shown in Figure 3. The model is suspended by springs to permit the free vibration of the model. The vertical damping of the system is 0.27% and the torsional damping is 0.15%. These values are below 0.3%, as required by JTGT 3360-01-2018 [23]. The tests were performed at a wind velocity ranging $U = [0.5, 10.5]$ m/s, leading to Reynolds numbers in the range of $Re = \left[1.835 \cdot 10^4, 3.968 \cdot 10^5\right]$, depending on the gap. Three acceleration sensors and displacement laser sensors were installed to monitor the model vibrations. The sampling frequency is 256 Hz, and the sampling duration for each case is 60 s. The sampling starts after the vibration of the segment model is stabilized.

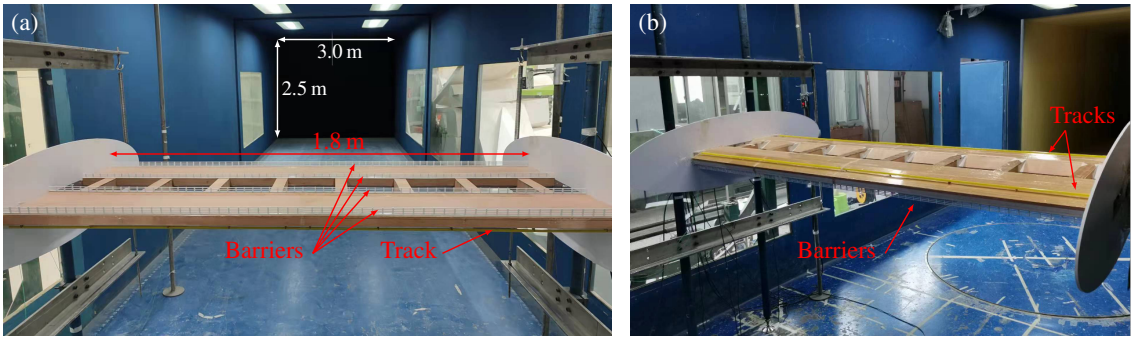

Figure 4: Sectional model in the wind tunnel test chamber at Chang'an University, Xi'an, China. Picture (a) shows a view of the model from the top, while (b) displays the model upside down to show the bridge overhaul vehicle tracks.

3.2. VIV performance objectives and acceptance criteria

VIV are undesired wind-induced responses that affect the performance of the bridge during its life-cycle (Hosomi et al. [26], Irwin [74]). International codes and standards impose thresholds to VIV responses (ASCE Committee on Cable-Stayed Bridges [22], JTGT 3360-01-2018 [23], ISO 2631 [24]), as well as project specifications (Stretto di Messina [25]). These limitations can have different natures, such as:

- Amplitude limitation, as required by JTGT 3360-01-2018 [23].
- RMS of acceleration limitation, as required in the Messina project specifications (Stretto di Messina [25]).

- Functionality and comfort performance requirements, typically related to driving comfort. A good example is the Sperling indicator (Garg and Dukkipati [75]), based on the peak amplitude and vibration frequency (Zhou et al. [40]).

- Fatigue strength design (see, for instance, Hosomi et al. [26], Pia Repetto and Solari [76], Chen [77]).

In this study, amplitude limitations on the VIV response will be used as described in the Code of Wind-resistant Design Specification for Highway Bridges (JTG/T 3360-01-2018) of China (JTGT 3360-01-2018 [23]), which is the governing standard for the bridge used as an application example. Hence, the amplitude of the vertical vortex-induced resonance A should satisfy:

$$A \leq \gamma_v \frac{0.04}{f_h}, \tag{5}$$

where f_h is the vertical frequency of the bridge, and γ_v is the coefficient of vortex-induced resonance, which is taken as 1.0 when the response is obtained using wind tunnel tests. It must be noted that the heaving amplitude is typically expressed as the non-dimensional term A/D. On the other hand, the amplitude of torsional vortex-induced resonance θ should satisfy

$$\theta \leq \gamma_v \frac{4.56}{B f_\theta}, \tag{6}$$

where f_θ is the torsional frequency, and B is the width of the bridge. The frequencies are provided in Table 2. Accordingly, the resulting limit values for the vortex vibration amplitude of the bridge

Table 2: Natural frequencies for different values of the gap distance C.

Deck cross-section			Vertical Bending frequency f_h		Torsional frequency f_θ	
C/D	C (Full bridge) [m]	C (Model) [mm]	Full bridge	Model	Full bridge	Model
0.714	2.8	40	0.122	3.418	0.327	9.155
1.429	5.6	80	0.122	3.418	0.323	9.033
2.143	8.4	120	0.122	3.418	0.314	8.789
2.857	11.2	160	0.122	3.418	0.305	8.545
3.571	14.0	200	0.122	3.418	0.296	8.301

are shown in Figure 5, where it can be seen that the limit for the non-dimensions vertical resonance A/D is 0.0837 mm and the limit for the torsional response θ ranges from 0.316° to 0.372° depending on the value of the gap distance C.

3.3. VIV response of the initial design

The torsional amplitude θ as a function of the reduced velocity U^* of the VIV of the initial design described in Section 3 is shown in Figure 6. It can be seen that the response is bimodal

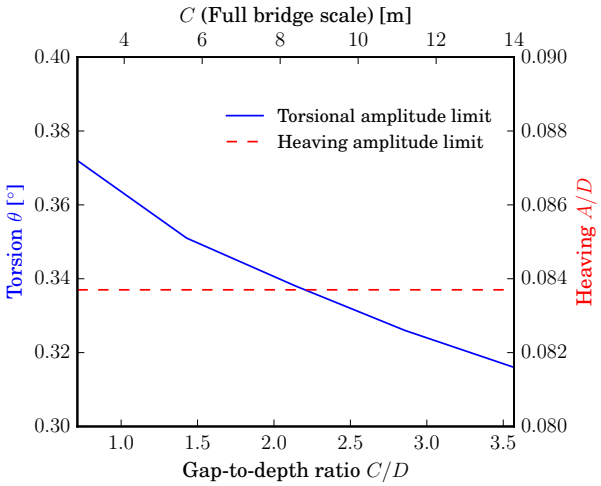

Figure 5: VIV limit values for the torsional and vertical degrees of freedom according to JTGT 3360-01-2018 [23] and the frequency values reported in Table 2.

with two prominent peaks, the first one in the range of reduced velocities $U^* = [5, 7.5]$, and the second one in $U^* = [11, 14.5]$. Similar responses will be reported in the forthcoming Sections for other candidate designs included in the shape design domain with slight variations in the range of reduced velocities for each peak. However, it can be generally assumed that the first peak occurs at reduced velocities $U^* < 10$, and the second peak is found at $U^* > 10$. Given that the peak values are the response used to drive the design optimization, two independent design constraints will be formulated for the amplitude of each peak and each degree of freedom to properly capture the sensitivity of each design variable with each peak amplitude. This facilitates the convergence of the gradient-based optimization algorithm and avoids switching the maximum value from one peak to another.

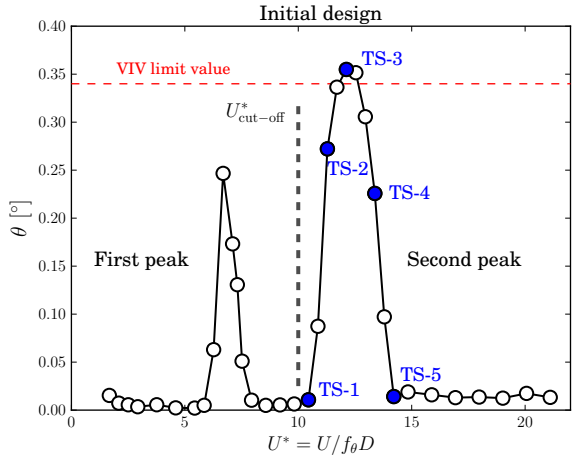

Figure 6: Torsional response as a function of the reduced velocity of the initial design defined in Figure 3 and Table 1. The time histories and spectra of the tests marked in blue for the second peak "TS-*i*" are given in Figure 7.

Figure 7 reports the time history of the torsional amplitude and the associated spectra for some

tests of the second peak "TS-i". Five time histories in the range of reduced velocities $U^* = [5, 10]$ are shown corresponding to the excitation starting ("TS-1"), occurrence ("TS-2"), peak ("TS-3"), descent ("TS-4"), and end ("TS-5"). Similar responses are found for other peaks and responses for other deck configurations reported in the paper.

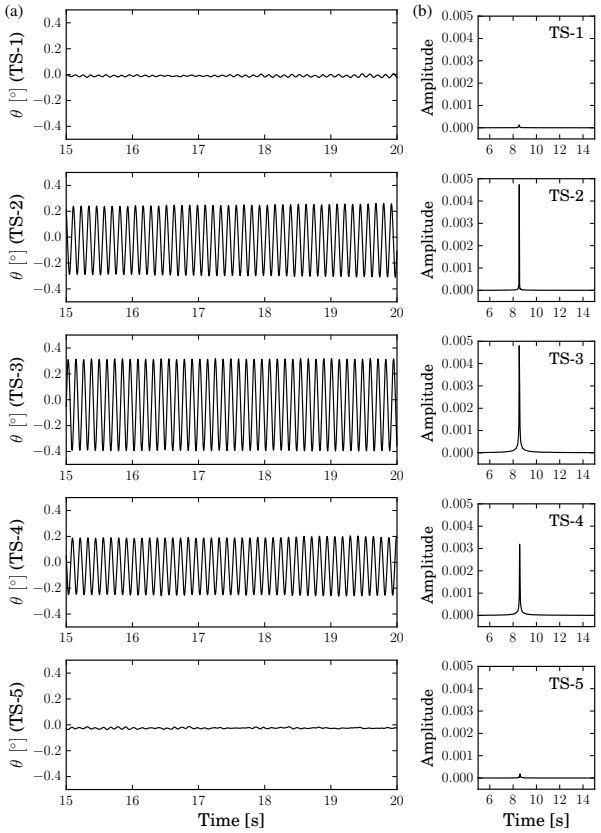

Figure 7: Time histories and spectra of torsional amplitude for specific values of reduced velocity U^* describing the second peak as indicated in Figure 6.

3.4. Specific formulation of the optimization problem

The specific formulation of the optimization problem for the application case described in Section 3 is discussed here. The objective function is analytically calculated as described in Section 3.5, while the VIV responses are obtained from the surrogate model (see Section 2.2). Given the bimodal response found in Section 3.3 for the VIV response of the initial design shown in Figure 6, a cut-off reduced velocity of $U^*_{\text{cut-off}} = 10$ is adopted to handle each peak responses by the adequate design variable, as discussed in Section 2.2. The selection of this value is explained in Section 3.3. Since the focus is on the vertical and torsional responses, four design constraints will be formulated in the optimization problem to control the VIV response along the design optimization process. Hence, $V_n = 4$ in Equation (1), which can be written for the specific application

case studied herein as:

$$
\begin{aligned}
&\text{find}: \mathbf{S}_d = (C, J)\,, \\
&\text{minimize}: F(C) \\
&\text{subject to}: \\
&\quad g^{VIV}_{\theta[U^*\leq 10]}(\mathbf{x}_s) = \frac{\theta[U^* \leq 10]}{\theta_{max}} - 1 \leq 0, \\
&\quad g^{VIV}_{\theta[U^*>10]}(\mathbf{x}_s) = \frac{\theta[U^* > 10]}{\theta_{max}} - 1 \leq 0, \\
&\quad g^{VIV}_{A/D[U^*\leq 10]}(\mathbf{x}_s) = \frac{A/D[U^* \leq 10]}{A/D_{max}} - 1 \leq 0, \\
&\quad g^{VIV}_{A/D[U^*>10]}(\mathbf{x}_s) = \frac{A/D[U^* > 10]}{A/D_{max}} - 1 \leq 0, \\
&\quad C^L \leq C \leq C^U, \\
&\quad J^L \leq J \leq J^U,
\end{aligned}
\tag{7}
$$

The selection of the most effective optimization engine is challenging due to the presence of multiple peaks and local minima in the response surfaces of the VIV responses as a function of the deck shape variables. While metaheuristic optimization algorithms (e.g. genetic algorithms (Holland [78], Wahde [79])) are conceived and expected to carry out an effective global exploration of the design domain, there is no guarantee of good performance and no mathematical proof that the solution obtained is a minimum. On the other hand, gradient-based optimization algorithms (Hernández [80]) guarantee the fulfillment of the Karush–Kuhn–Tucker (KKT) convergence conditions (Kuhn and Tucker [81]), i.e. the identification of a minimum and, consequently, an optimum design. In this study, the optimization algorithm selected is the Quadratic Sequential Programming (SQP) algorithm (Haftka and Gürdal [82], Arora [83]). The SQP method is a constrained optimization gradient-based algorithm that creates an approximated problem by substituting the objective function with a quadratic function and linearizing the constraints. This approximation is iteratively solved until convergence. This methodology is very efficient and shows a great performance in the application case reported in this study. It can be found in several optimization packages, such as GENESIS (Van [84]), OptiStruct (Alt [85]), DOT (Research and Development [86]), and MATLAB (The [87]).

3.5. Objective function F: deck construction cost

Changing the deck cross-section configuration impacts the bridge construction and maintenance costs. One of the key parameters affecting the costs is the gap distance between boxes, which makes the construction cost grow with the gap (Trein et al. [16]). This increase in construction costs impacts the identification of the optimum deck cross-section. While increasing the gap may be beneficial to improve the aeroelastic performance (Qin et al. [12], Kwok et al. [13]), the

optimum design will be identified by minimizing the economic cost while fulfilling all the performance specifications formulated as design constraints (Cid Montoya et al. [61, 62]). In this study, actual 2021 construction costs of the bridge deck as a function of the gap distance are used in the optimization problem to define the objective function F (see Equation (1)). The cost model of the bridge deck in full scale is given by:

$$F_{\text{abs}}(C) = 3.091 \cdot C + 121.843, \tag{8}$$

where F_{abs} is the objective function expressed in millions of dollars \$M and C is the gap distance expressed in full scale in m. This equation is valid for the range of gaps considered in this study $C = [2.8, 14.0]$ m. The impact of the location of the track J on the bridge costs is negligible. Hence, the objective function is only a function of the gap $F(C)$. The objective function can also be expressed as a relative value F_{rel} of the maximum cost, which is \$165.126 for the maximum gap $C^U = 14.0$ m ($C/D = 3.571$), and as a function of the non-dimensional gap C/D as follows:

$$F_{\text{rel}}(C/D) = 0.073401 \cdot C/D + 0.737867. \tag{9}$$

The relationship of the cost with the gap is graphically shown in Figure 8.

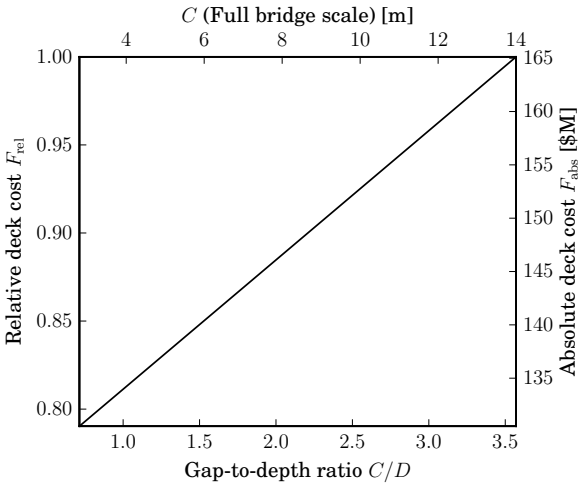

Figure 8: Relative and real construction costs of the bridge as a function of the gap distance between boxes.

4. Deck shape optimization

The optimization problem formulated in Section 3.4 for the application case described in Section 3 is solved herein using the methodology described in Figure 2. The global sampling carried out in the first cycle is reported in Section 4.1 and used to train the surrogate model described in Section 4.2. The quality of the surrogate to emulate the nonlinear behavior of the VIV response

in this application case is checked in Section 4.3, and the first cycle optimization carried out is reported in Section 4.4. Then, a second cycle is carried out to increase the accuracy of the surrogate in the neighborhoods of the solution of the optimum obtained in the first cycle, as described in Figure 2. Section 4.5 reports the second round of wind tunnel tests performed to update the surrogate and Section 4.6 describes the second cycle optimization. Finally, the optimum design is compared with the initial design in Section 4.7 to show the achievements of the proposed methodology.

4.1. Global sampling and VIV responses in the entire design domain (Cycle 1)

This study uses a full factorial sampling strategy to reduce the model construction cost and workload associated with intensive wind tunnel tests, as discussed in Section 2.3. A critical parameter to define when carrying out this sampling strategy is the number of samples and the sampling stratification step adopted for each design variable included in the design domain. The influence of the gap-to-depth ratio on the aeroelastic responses has been studied experimentally by several authors for twin-box (Chen et al. [88], Camera et al. [89], Xu et al. [90]) and multi-box decks (Andersen et al. [91]). Most of those studies focused on the gap as the only design variable. They systematically modified it by adopting gap steps ranging from 0.428 in Laima and Li. [20], to values higher than 4 (Trein et al. [16]). The most common step ratio is in the range $\Delta_{C/D} = [1.5, 2.0]$ (Qin et al. [12], Kwok et al. [13], Yang et al. [41]). Table 3 provides the deck geometry, the aeroelastic phenomena, and gap-to-depth ratios studied in some relevant contributions available in the literature. However, other geometrical parameters, such as the deck shape (Argentini et al. [11], Wang et al. [18], Kroon et al. [92]), and the location, shape, and size, of appendages, such as barriers (Bai et al. [42], Buljac et al. [64]), maintenance rails (Ge et al. [9]), and countermeasures (Bai et al. [38], Zhou et al. [40]) impact the aeroelastic responses. Given the large number of potential combinations involving multiple appendages, there are limited studies in the literature dedicated to systematically studying each case. Hence, there needs to be more previous experience with reasonable values for the maintenance rails location step. In the present study, we perform a full factorial sampling to consider the impact of the two design variables simultaneously. The gap step for the sampling plan of 0.714, which is lower than the ones adopted in most of the specific experimental studies focusing on the gap effect, as summarized in Table 3, and an average step for the normalized position of the maintenance rail of 0.248. A cross-validation study is later conducted in Section 4.3 to analyze the impact of the sampling resolution and the step adopted for J on the emulation of the VIV responses.

Based on the above discussion, twenty deck configurations are included in the global sampling plan of the first cycle (see Figure 2), corresponding to five different gap-to-depth ratios $C/D = [0.714, 1.429, 2.143, 2.857, 3.571]$ with four different locations for the maintenance track $J/b = [0.162, 0.424, 0.623, 0.908]$, as shown in Figure 9. In full scale, those dimensions are to $C =$

Table 3: Gap-to-depth values and step ratios adopted in some representative experimental studies reported in the literature.

Reference	Bridge	Response studied	Gaps-to-depth ratios tested [E]	Step ratio [*]
Sato et al. [93]	Generic (bare)	Flutter	0.000, 1.700, 3.400, 5.100, 6.800, 8.500	1.700
Qin et al. [12]	Stonecutters (bare)	Flutter	0.000, 0.273, 2.114, 4.045, 5.977	1.902
Kwok et al. [13]	Stonecutters (bare)	Static & VIV	0.000, 0.286, 2.143, 4.086, 6.029	1.914
Chen et al. [88]	Stonecutters (bare)	Static (pressure, flow)	0.850, 1.700, 2.550, 3.400	0.850
Trein et al. [16]	Rectangular boxes (bare)	Static & Flutter	0.000, 1.000, 2.500, 5.000, 10.000, 15.000, 20.000, 30.000	4.286
Yang et al. [94]	Generic box (bare)	Flutter	0.000, 1.560, 3.120, 4.679, 6.239, 7.799	1.560
Yang et al. [14]	Generic box (bare)	Static & Flutter	0.000, 2.800, 5.600, 8.400, 11.200, 14.000	2.800
Laima and Li. [20]	Xihoumen (bare)	Static & VIV (flow)	0.000, 0.855, 1.283, 1.710, 2.138, 2.566, 2.993, 3.421, 5.986, 7.697, 10.260	0.428
Yang et al. [15]	Xihoumen (final)	VIV	0.000, 1.709, 3.419, 5.128, 6.838, 8.547	1.709
Yang et al. [41]	Generic (bare)	Static & Flutter	0.000, 1.619, 3.214, 4.833, 6.429, 8.048	1.619
Nieto et al. [95]	Stonecutters (bare)	Static & Flutter	0.000, 0.280, 2.080, 3.960, 7.480	1.870
Tophøj and Hansen [96]	Slotted flat plate (bare)	Flutter	0.000, 0.250, 0.500 [H]	-
Wang et al. [19]	Xihoumen (bare)	Static & Buffeting	0.436, 1.219, 2.571, 3.554	1.039
Xu et al. [90]	Generic (final)	Static & VIV	0.125, 0.725, 1.675	0.775
Camera et al. [89]	Generic (wind screens)	Static & Flutter	0.000, 0.500, 1.000, 1.500, 2.000, 2.500, 3.000	0.500
Present study	Deck with appendages	VIV	0.714, 1.429, 2.143, 2.857, 3.571	0.714

[*] Representative value obtained as an average or the most repeated step value.
[E] Only the configurations experimentally studied using wind tunnel tests are listed.
[H] Gaps expressed as C/B since the research studies slotted flap plates.

$[2.8, 5.6, 8.4, 11.2, 14.0]$ m and $J = [2.810, 7.344, 10.794, 15.719]$ m, respectively. The initial design $\mathbf{S}_{d,0}$ described in Section 3 is included in the sampling plan and corresponds to design C_4J_2 (Sample S1-9) (see Table 4). The transversal beams are changed for each gap distance C when the model is adapted for each deck configuration. The barriers and the cross-section of the boxes are not modified during the tests to keep the geometric similitude.

The measured responses for the 20 designs are represented in Figure 10. The plots on the left side show the torsional amplitudes, while the non-dimensional vertical amplitudes (divided by the deck depth D) are displayed on the right column. Each row represents one value of the variable J, while variations in C are compared in each plot. Another advantage of using full factorial sampling strategies is that it facilitates the interpretation of the results and anticipates some trends that will be later seen in the response surfaces created by the surrogate model. The comparison shown in Figure 10 certifies the adequacy of the selection of the cut-off reduced velocity $U^*_{\text{cut-off}} = 10$ for this application example within the selected design domain. The responses are compared with the maximum admissible values provided in Figure 5, which is represented with a red dashed line. The maximum value of each peak is the value that will be used in the design optimization process. Hence, the peak values are the quantities used to train the surrogate model. A complete list of the peak values is provided in Table 4.

4.2. Global surrogate model (Cycle 1)

Four responses must be emulated by the surrogate model as discussed in Section 3.3 (Equation (4)), which are the (1) non-dimensional vertical amplitude for the peak at reduced velocities before the cut-off reduced velocity $A/D\,(U^* \leq 10)$; (2) the second vertical peak at high reduced

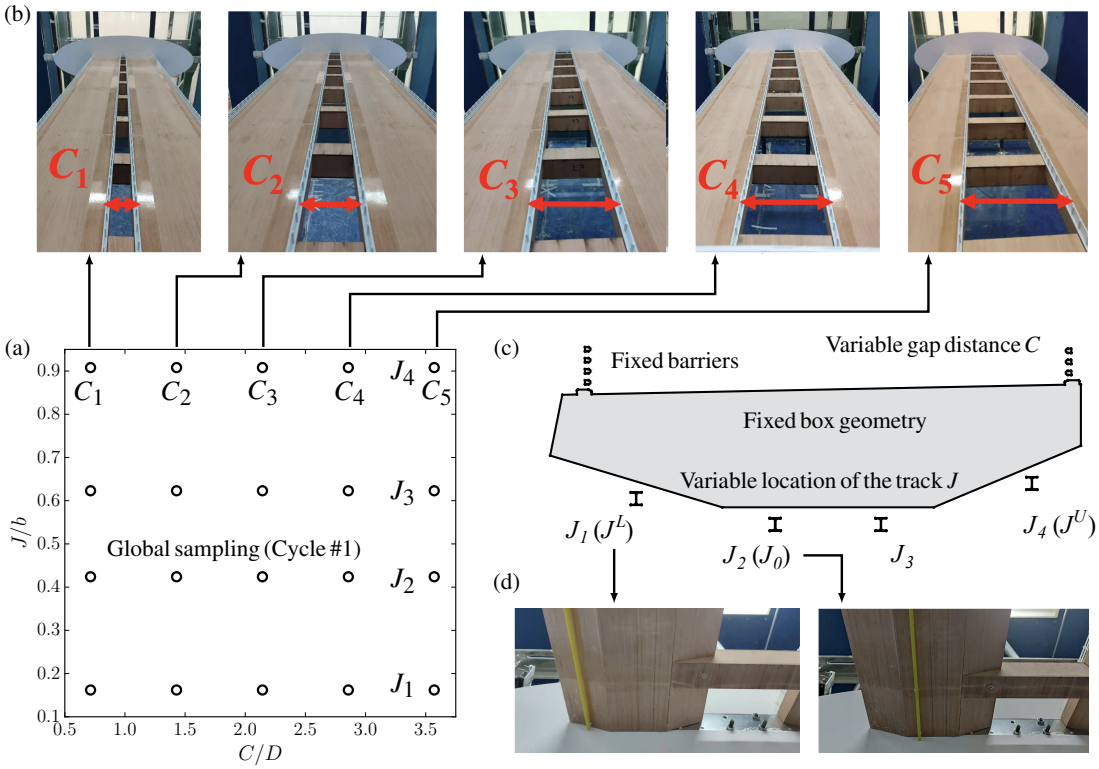

Figure 9: Global sampling plan carried out for building the VIV emulator in the first cycle of the optimization process. (a) Sampling plan which the shape design domain, (b) Pictures of the sectional model with five different gap distances, (c) positions of the maintenance track considered in the sampling plan, and (d) detailed pictures of some positions of the maintenance track.

Table 4: Summary of the maximum values found in the VIV responses in the ranges $U_1^* = [0, 10]$ and $U_2^* = [10, \infty]$.

Sample		Deck design		Torsion		Heaving	
Number	Name	C/D	J/b	$\theta\,[^\circ]\,(U^* \leq 10)$	$\theta\,[^\circ]\,(U^* > 10)$	$A/D\,(U^* \leq 10)$	$A/D\,(U^* > 10)$
S1-1	C_1J_1	0.714	0.162	0.0194	0.0096	0.0002	0.0016
S1-2	C_2J_1	1.429	0.162	0.0286	0.0596	0.0103	0.0021
S1-3	C_3J_1	2.143	0.162	0.1949	0.0559	0.0906	0.0016
S1-4	C_4J_1	2.857	0.162	0.2692	0.1385	0.0926	0.0021
S1-5	C_5J_1	3.571	0.162	0.0563	0.0131	0.0019	0.0019
S1-6	C_1J_2	0.714	0.424	0.0598	0.0314	0.0004	0.0017
S1-7	C_2J_2	1.429	0.424	0.0277	0.0282	0.0399	0.0025
S1-8	C_3J_2	2.143	0.424	0.1289	0.0156	0.0765	0.0027
S1-9	C_4J_2 ($\mathbf{S}_{d,0}$)	2.857	0.424	0.2466	0.3549	0.0870	0.0037
S1-10	C_5J_2	3.571	0.424	0.0734	0.4079	0.0936	0.0027
S1-11	C_1J_3	0.714	0.623	0.0084	0.0081	0.0608	0.0019
S1-12	C_2J_3	1.429	0.623	0.0080	0.0148	0.1010	0.0035
S1-13	C_3J_3	2.143	0.623	0.0333	0.2010	0.1524	0.0112
S1-14	C_4J_3	2.857	0.623	0.2599	0.2451	0.1839	0.0116
S1-15	C_5J_3	3.571	0.623	0.2553	0.0149	0.1226	0.0031
S1-16	C_1J_4	0.714	0.908	0.0038	0.0054	0.0004	0.0017
S1-17	C_2J_4	1.429	0.908	0.0078	0.0092	0.0005	0.0030
S1-18	C_3J_4	2.143	0.908	0.0580	0.0931	0.0008	0.0200
S1-19	C_4J_4	2.857	0.908	0.1381	0.2512	0.0295	0.0031
S1-20	C_5J_4	3.571	0.908	0.1369	0.0106	0.0010	0.0028

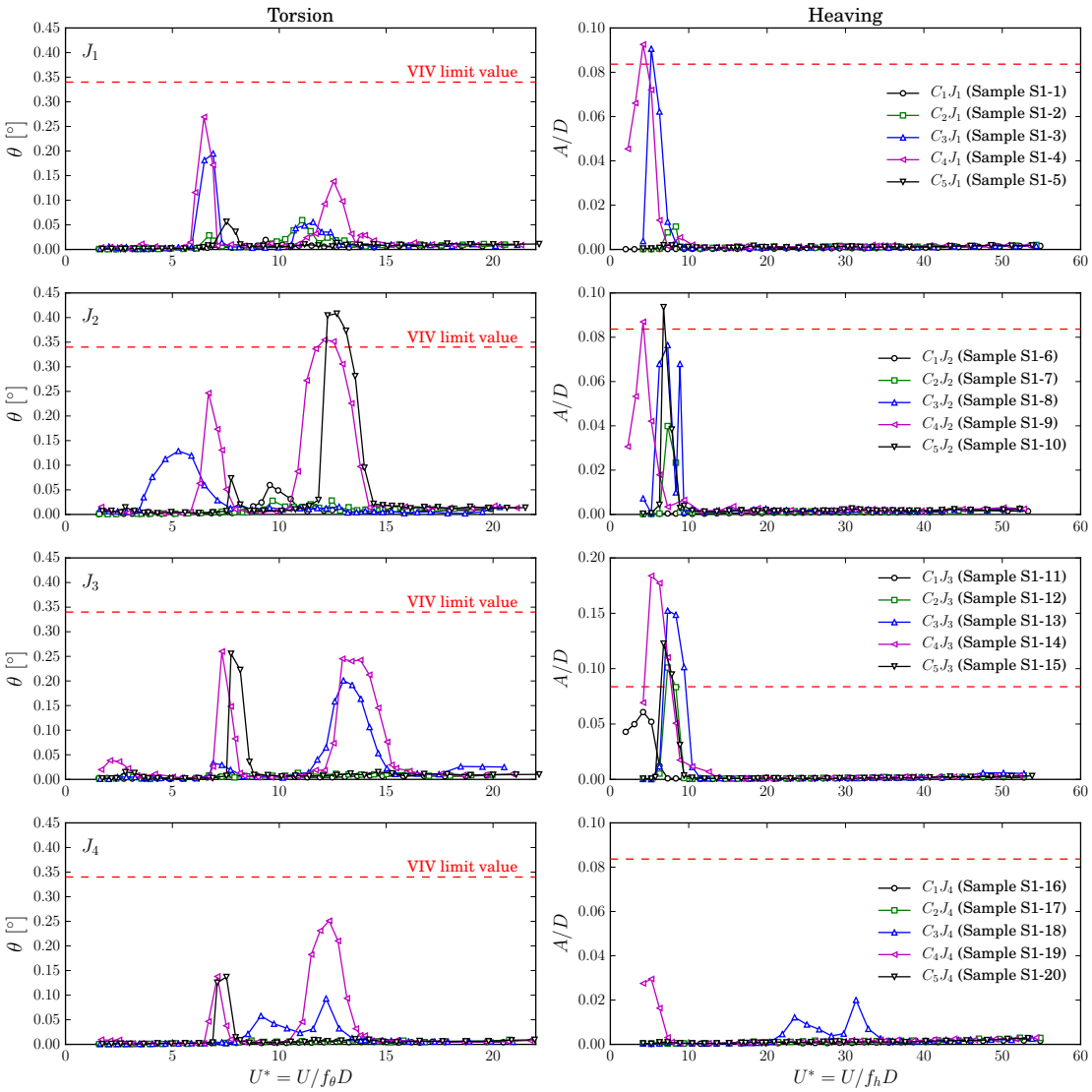

Figure 10: Comparison of the VIV responses of the designs considered in the first batch of samples shown in Figure 9. The red dashed line indicates the maximum admissible value according to JTGT 3360-01-2018 [23] (see Section 3.2).

velocities $A/D\,(10 > U^*)$; (3) the torsional amplitude for low reduced velocities $\theta\,(U^* \leq 10)$; and (4) and the second peak of the torsional response $\theta\,(10 > U^*)$. The input of the model is the deck shape $\boldsymbol{S}_d$, which is defined by the two shape design variables J and C. Hence, the formulation of the model from a black-box perspective can be written as follows:

$$\mathcal{V}\,(\boldsymbol{S}_d) = \left[A/D\,(U^* \leq 10)\,, A/D\,(10 > U^*)\,, \theta\,(U^* \leq 10)\,, \theta\,(10 > U^*)\right]. \tag{10}$$

A Kriging surrogate model is trained using the information reported in Table 4, giving place to the response surfaces shown in Figure 11. The limits adopted for the vertical and torsional responses discussed in Section 3.2 are also plotted in Figure 11 in order to identify the feasible and unfeasible design regions. It can be seen that the responses that are going to condition the VIV-resistant design of the bridge deck are the vertical displacements for low reduced velocities and the torsional vibrations for reduced velocities higher than 10. The vertical response for $U^* > 10$ shows a very low amplitude that does not affect the aeroelastic design of the bridge. In general, the lower amplitudes are found for low values of the gap distance C. The role of variable J in the creation of vortices is harder to anticipate and highly conditioned by the value of the gap distance C. This can be seen in Figure 12 for the response $A/D\,(U^* \leq 10)$, where it is clear that the feasible design domain drastically changes for each value of C. This fact remarks the importance of considering all shape design variables simultaneously during holistic design processes. However, it can be seen in Figure 11 that medium values of J, which means that the rail is located at the center of the bottom plate of the deck (see Figure 3), cause the higher amplitudes in both vertical and torsional responses.

4.3. Cross-validation and surrogate model update (Cycle 1)

The relationship of the VIV responses with the shape design variables is expected to be strongly irregular due to the nonlinear nature of bluff body aerodynamics. Hence, a cross-validation study is carried out to quantify this effect in the context of the current application example. This step is not included in the flowchart shown in Figure 2 because it is not necessary for the optimization process. However, we carry out this validation to further guarantee the robustness of the procedure. In particular, we set the focus on the effect of the position of the maintenance track on the VIV responses. With this aim, three new designs were tested in the CA-1 Wind Tunnel Laboratory of Chang'an University, consisting of changing the value of J for a given fixed value of C to keep the factorial sampling strategy. The gap-to-depth ratio chosen is $C/D = 2.857$, and the positions of the track are $J/b = [0.243, 0.524, 0.822]$, which corresponds to $J = [4.215, 9.069, 14.244]$ m in full scale. Hence, the track position step is notably reduced. These designs are added to the original sampling plan in Figure 13 as red squares.

The results of the tests are shown in Figure 14, and the peak values are summarized in Table 5.

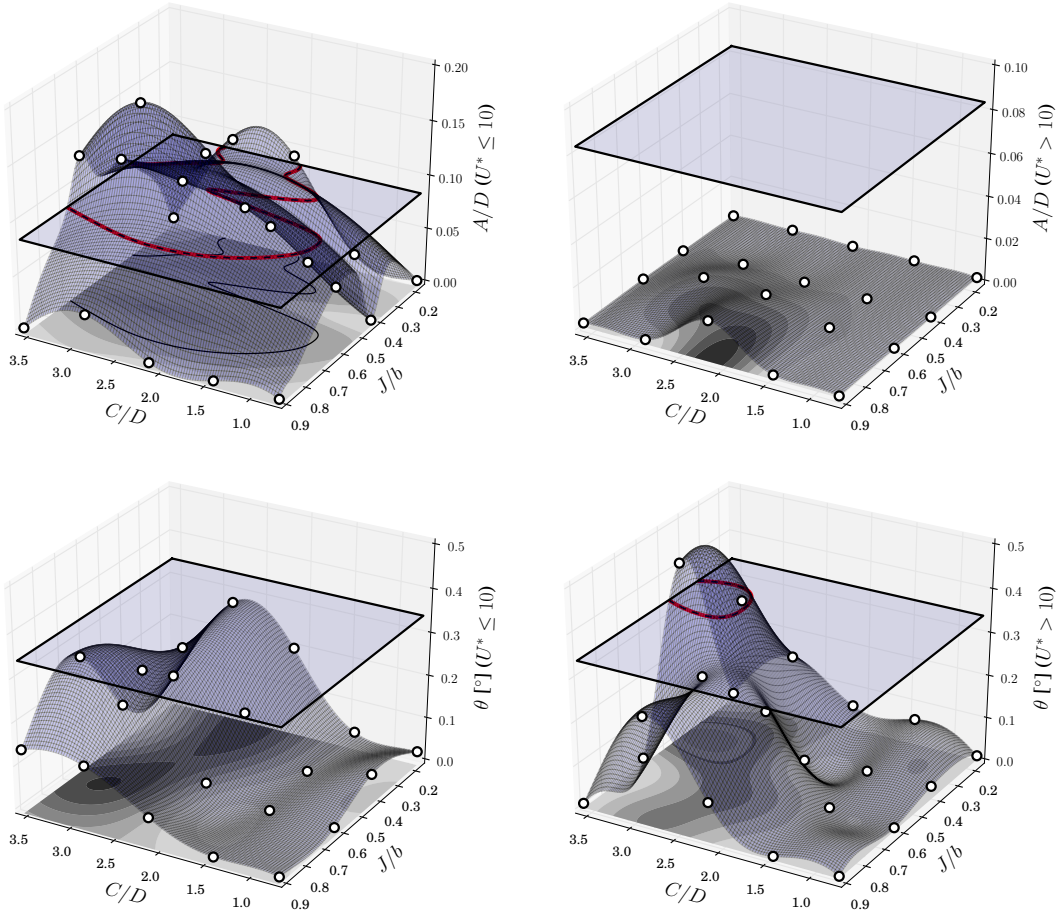

Figure 11: Response surfaces provided by the surrogate model as a function of the deck shape design variables expressed as non-dimensional values (C/D and J/b) for the four output responses ($A/D\,(U^* \leq 10)$, $A/D\,(10 > U^*)$, $\theta\,(U^* \leq 10)$, and $\theta\,(10 > U^*)$) trained with the information obtained in the first sampling reported in Table 4 (white circles). The intersection (red line) of the response surfaces (blue surfaces) with the limit values reported in Figure 5 (horizontal plane) permit the identification of the feasible and unfeasible regions of the design domain (black continuous line).

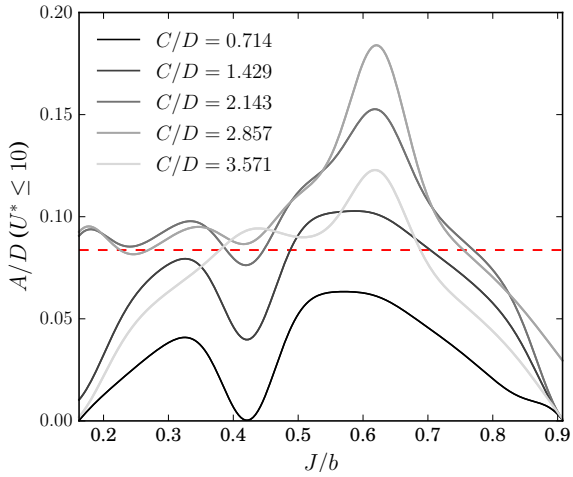

Figure 12: Response $A/D\,(U^* \leq 10)$ provided by the surrogate model for several values of G/D as a function of J/b. The VIV limit value (JTG/T 3360-01-2018) is shown in red to highlight the impact of the gap distance C on the sensitivity of the response $A/D\,(U^* \leq 10)$ with the track position J.

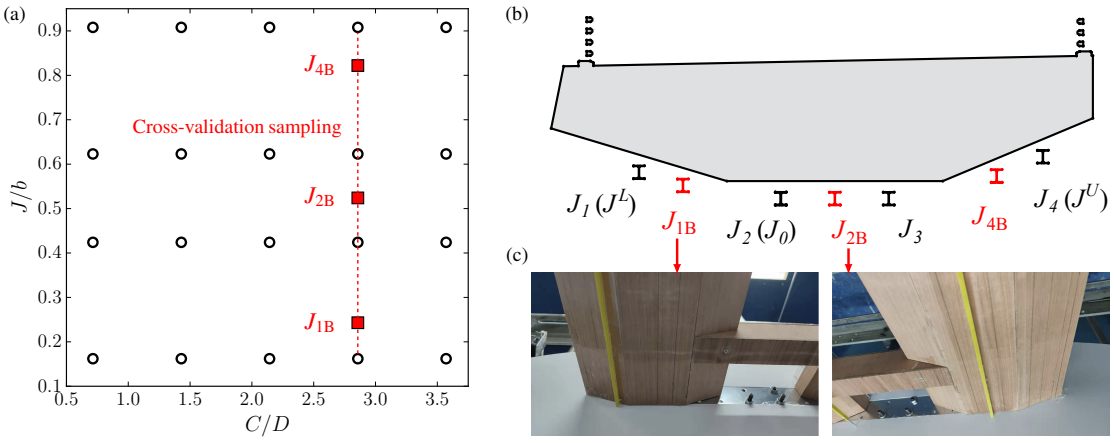

Figure 13: Updated sampling plan with the samples used in the cross-validation. (a) Full set of samples used in Cycle #1 with the new samples (C_4J_{1B}, C_4J_{2B}, and C_4J_{4B}) represented as red squares, (b) detail of the locations of the maintenance tracks for the new designs, and (c) Pictures of the sectional models tested for the cross-validation sampling.

In most cases, the results obtained follow the trend anticipated by the surrogate model shown in Figure 11. However, the value obtained for the design C_4J_{1B} (Sample CV-21) shows that the surrogate was overestimating the vertical response of the first peak ($A/D\,(U^* \leq 10)$), while slightly underestimated the value for the other three responses. However, the surrogate was underestimating the second torsional peak of the designs C_4J_{4B} (Sample CV-23), which violated the limit imposed by the JTG/T 3360-01-2018 code.

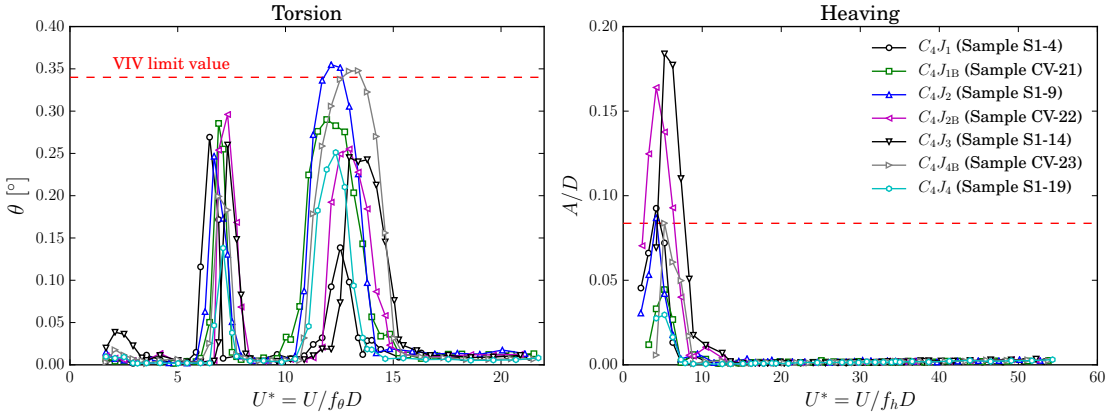

Figure 14: Comparison of the VIV responses of the designs considered in the cross-validation for geometries for C_4, as shown in Figure 9.

Table 5: Summary of the maximum values found for the VIV responses after the extra wind tunnel tests performed for the cross-validation. The gap-to-depth ratio adopted is $C/D = 2.857$. Numeration of the samples following Table 4.

Sample		Deck design		Torsion		Heaving	
Number	Name	C/D	J/b	$\theta\,[°]\,(U^* \leq 10)$	$\theta\,[°]\,(U^* > 10)$	$A/D\,(U^* \leq 10)$	$A/D\,(U^* > 10)$
CV-21	C_4J_{1B}	2.857	0.243	0.2855	0.2901	0.0445	0.0033
CV-22	C_4J_{2B}	2.857	0.524	0.2961	0.2552	0.1640	0.0104
CV-23	C_4J_{4B}	2.857	0.822	0.1992	0.3478	0.0837	0.0029

Given the relevant cost of wind tunnel testing and the valuable information provided by the new samples, the surrogate model is updated by including the new data in the training process. A comparison of the two surrogates is provided in Figure 15, where the impact of the new samples on the surrogate trend can be clearly seen, and a complete view of the four response surfaces is shown in Figure 16. As previously discussed, the most significant contribution of the new samples is the updated response surface for the second torsional peak since Sample CV-23 noticeably reduces the feasible design domain, at least for values of C/D around 2.857. On the other hand, Sample CV-21 provides valuable information to determine if that region is part of the feasible design domain and, therefore, if the designs in that region are acceptable candidate designs. It must be remarked that the number and distribution of samples is always conditioned by the specific application example

and the size of the design domain. For this reason, the methodology proposed in this study carries out a second cycle that refines the sampling plan in the neighborhood of the solution found by the optimization algorithm in the first cycle to guarantee that the real optimum fulfills all the design requirements imposed in the design problem.

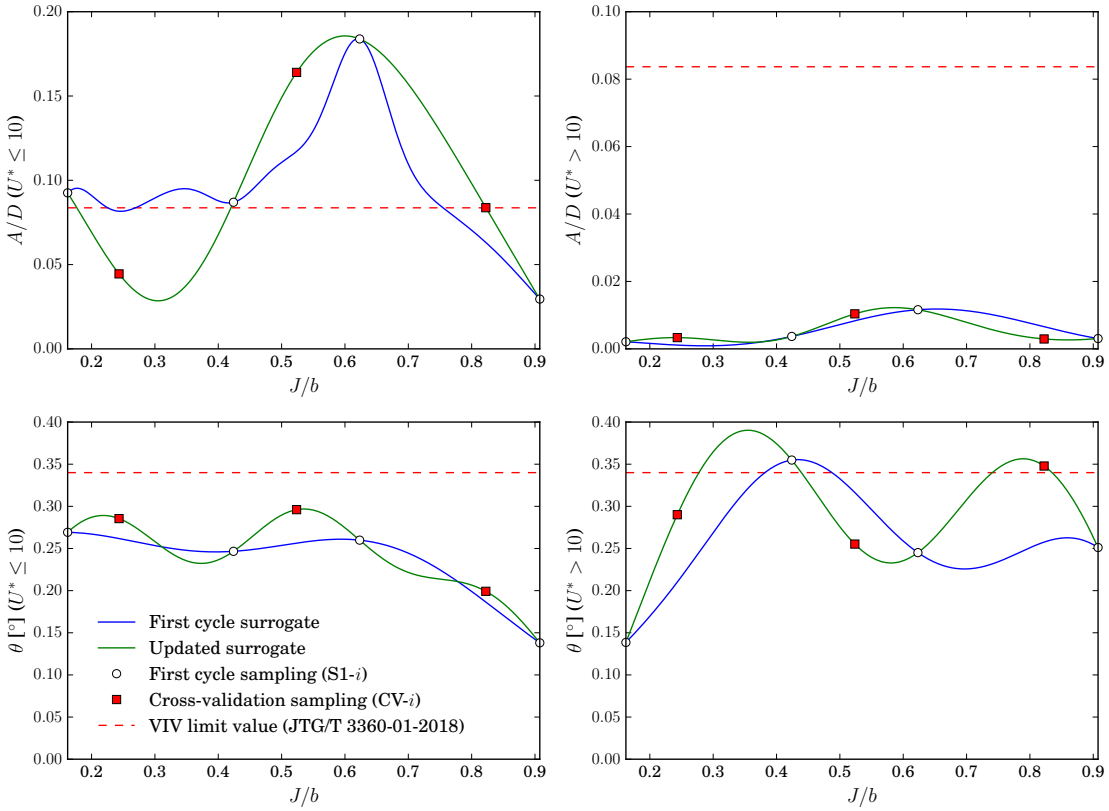

Figure 15: Comparison of the responses emulated by the original surrogate (in blue) and the updated surrogate with the new samples (in green). The curve shown is the value of the response surface as a function of J for a fixed value of $C/D = 2.857$.

4.4. First cycle optimization (Cycle 1)

The optimization problem formulated in Equation (7) seeks the minimization of the cost of the bridge, modeled in Figure 8, while keeping the VIV responses, emulated by the VIV surrogate shown in Figure 16, under the imposed threshold. The updated surrogate is shown in Figure 16, where it can be seen that the only responses that are active in the optimization problem are the first vertical peak and the second torsional peak. In both cases, significant responses are found for large values of C, i.e., large gap distances. Also, the value of J, i.e., the track's location, profoundly influences all the responses. However, it can be anticipated that low values of C result in low VIV responses.

On the other hand, it is crucial to understand the economic model to determine the more efficient designs from the cost perspective. As discussed in Section 3.5, the cost is linear with the value of C due to the cost of the transversal beams that link the boxes, as also investigated in

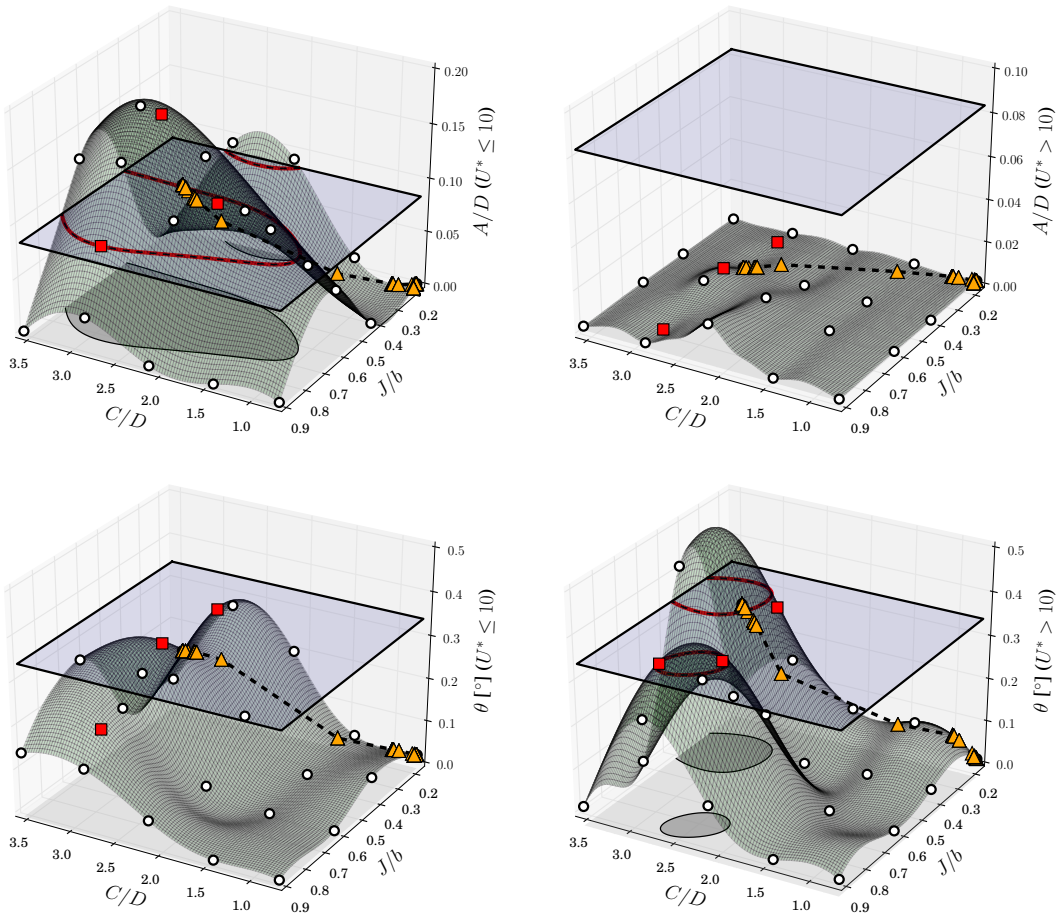

Figure 16: Response surfaces provided by the updated surrogate model (green surfaces) built from the information obtained in the first sampling (white circles) and the new samples used for the cross-validation analysis (red squares). New sampling data taken from Table 5. The convergence of the optimization is represented using a continuous black line with orange triangular markers. The unfeasible design domain is shown with a gray shadow delimited by a black continuous line.

Cid Montoya et al. [61]. Conversely, J has no relevant impact on the cost. This is represented in Figure 17 along with the intersection of the response surfaces reported in Figure 16 with the imposed thresholds, which helps to identify the feasible and unfeasible design domains. The convergence path of the optimization is shown in Figure 16 and Figure 17 as a dark line with yellow triangles, representing the iterations of the optimization algorithm. The optimum design is marked with a yellow star, corresponding to design $C/D = 0.714$ and $J/b = 0.181$.

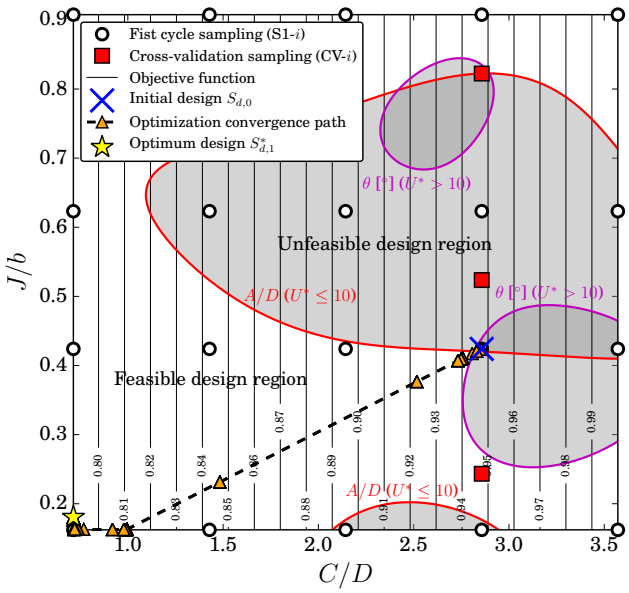

Figure 17: Convergence of the surrogate-based optimization within the design domain. The objective function F (black thin lines) and the boundaries of the VIV design constraints that can condition the design during the optimization process ($A/D\,(U^* \leq 10)$ (red) and $\theta\,(U^* > 10)$ (pink)) are shown using contour surfaces.

4.5. Local sampling in the neighborhoods of the first cycle optimum design (Cycle 2)

The highly nonlinear relationship of the VIV response with deck shape design variables makes the sampling plan a critical step to capture all the aerodynamic features, as discussed in Section 4.3. Since each sample involves a high economic cost and intensive workload, it is impossible to carry out a large number of samples that permit an accurate exploration of the entire design domain. Alternatively, design space exploration efforts must focus on the design regions with competitive candidate designs. Hence, we propose in the methodology outlined in Figure 2 to carry out sequential updates of the VIV surrogate model in the neighborhoods of the solution of the previous cycle. In this manner, the optimization algorithm can safely converge to the optimum design, avoiding the risk of considering designs far from tested ones. This was the reason for selecting a Kriging surrogate to emulate the VIV response since this model guarantees that it reproduces the responses of all samples used in the training process.

The new batch of samples added to the original sampling plan include three new designs around the optimum design found in the first cycle (Figure 17). Figure 18 shows the updated

sampling plan with the new three samples as blue circles around the first cycle optimum design indicated as a yellow star. The new designs are reported in Table 6, which includes a new gap-to-depth ratio $C/D = 1.000$ (3.9 m in full scale) and a new position of the track $J/b = 0.237$ (4.101 m in full scale). The natural frequencies of the new designs when $C/D = 0.714$ were reported in Table 2, while the torsional frequency for $C/D = 1.000$ is 9.1 Hz for the sectional model and 0.325 at the full bridge scale. Consequently, their torsional limits for these gap distances are 0.372° and 0.364°, respectively, which would update the limits specified in Figure 5. The experimental VIV responses obtained for the four designs in the neighborhood of the optimum design obtained in the first cycle are reported in Figure 19, where it can be seen that no VIV peaks are developed for those designs. Table 6 reports the maximum values found for the four responses for the new designs. It can be seen that the values are far from the limit, which guarantees that the designs in the neighborhoods of the solution are not prone to suffer VIV.

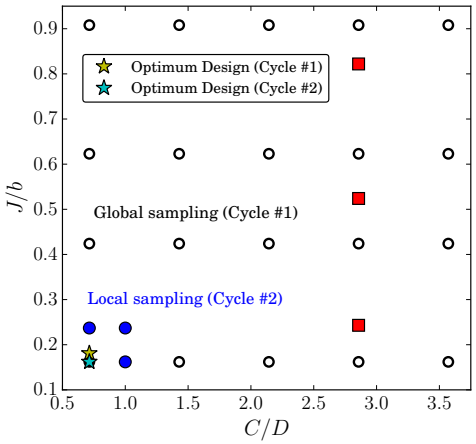

Figure 18: Sampling plan carried out in Cycle #2 with a local focus in the neighborhoods of the optimum design obtained in Cycle #1.

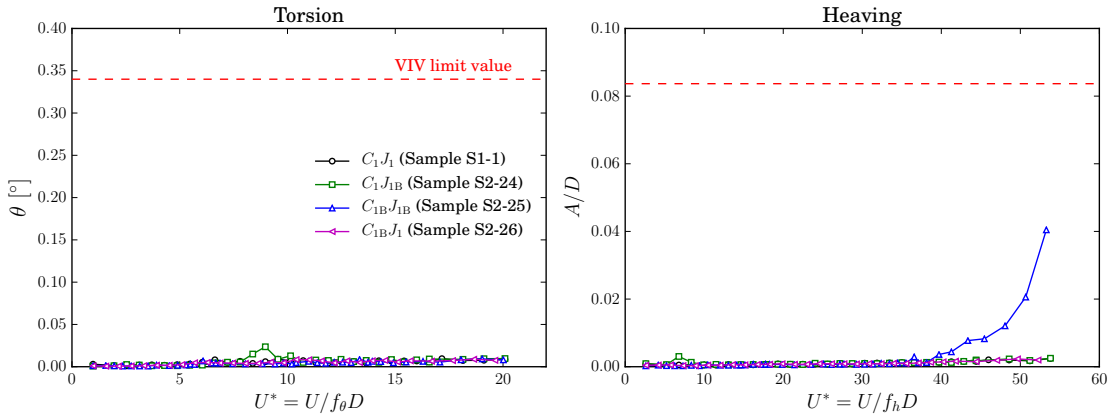

Figure 19: VIV responses of the new designs tested in teh wind tunnel as described in Figure 18.

The Kriging surrogate is updated with the information reported in Table 6, giving place to the new response surfaces shown in Figure 20. There are no relevant changes in the torsional

Table 6: Summary of the maximum values found for the VIV responses for the new samples tested for the second cycle of the optimization process. Numeration of the samples following Table 4 and Table 5.

Sample		Deck design		Torsion		Heaving	
Number	Name	C/D	J/b	$\theta[^\circ](U^* \leq 10)$	$\theta[^\circ](U^* > 10)$	$A/D\,(U^* \leq 10)$	$A/D\,(U^* > 10)$
S2-24	C_1J_{1B}	0.714	0.237	0.0236	0.0129	0.0030	0.0025
S2-25	$C_{1B}J_{1B}$	1.000	0.237	0.0068	0.0092	0.0005	0.0405
S2-26	$C_{1B}J_1$	1.000	0.162	0.0054	0.0088	0.0005	0.0023

responses and first vertical peak, which are the responses that can impact the optimum design. However, the second vertical peak response surface is substantially changed, given the relatively high value reported for sample S2-25. Nevertheless, this modification in the surrogate model does not impact the design process since this value is still far from the vertical limit.

4.6. Second cycle optimization (Cycle 2)

Once the VIV surrogate model is updated with the new samples to increase the local accuracy in the neighborhoods of the solution of the first cycle, a second optimization is carried out to guarantee the complete convergence of the outer loop of the methodology described in Section 2. Figure 21 shows the convergence of the two optimizations performed in each cycle. In the first cycle, the objective function F was reduced from 0.947 to 0.79 after 19 iterations, thanks to the reduction in the gap distance. The optimization conducted in the second cycle carried out 11 iterations and slightly modified the optimum design based on the new information provided by the updated surrogate model. The optimum design was slightly modified due to the null slope in the J direction.

Table 7 reports the evolution of the deck design, from the initial design $\boldsymbol{S}_{d,0}$ to the optimum design found in the second cycle $\boldsymbol{S}^*_{d,2}$. The surrogate model emulates the values reported in this table for the VIV responses. The initial and optimum design of the second cycle coincides with the wind tunnel tests, given that Kinging surrogates reproduce the same value as the samples used in the training process. This also avoids another round of iterations since the optimum design was already tested in the initial set of samples tested to build the surrogate. Hence, experimental proof exists that the optimum design does not develop VIV.

4.7. Optimum design

Figure 22 compares the initial and optimum design configurations obtained after two cycles of the data-driven surrogate-based design optimization process. As shown in Figure 22 (b) and (c), the VIV response was mitigated entirely by shaping the bridge deck, even though both the torsional and vertical responses of the initial design violated the design constraints. The gap distance was

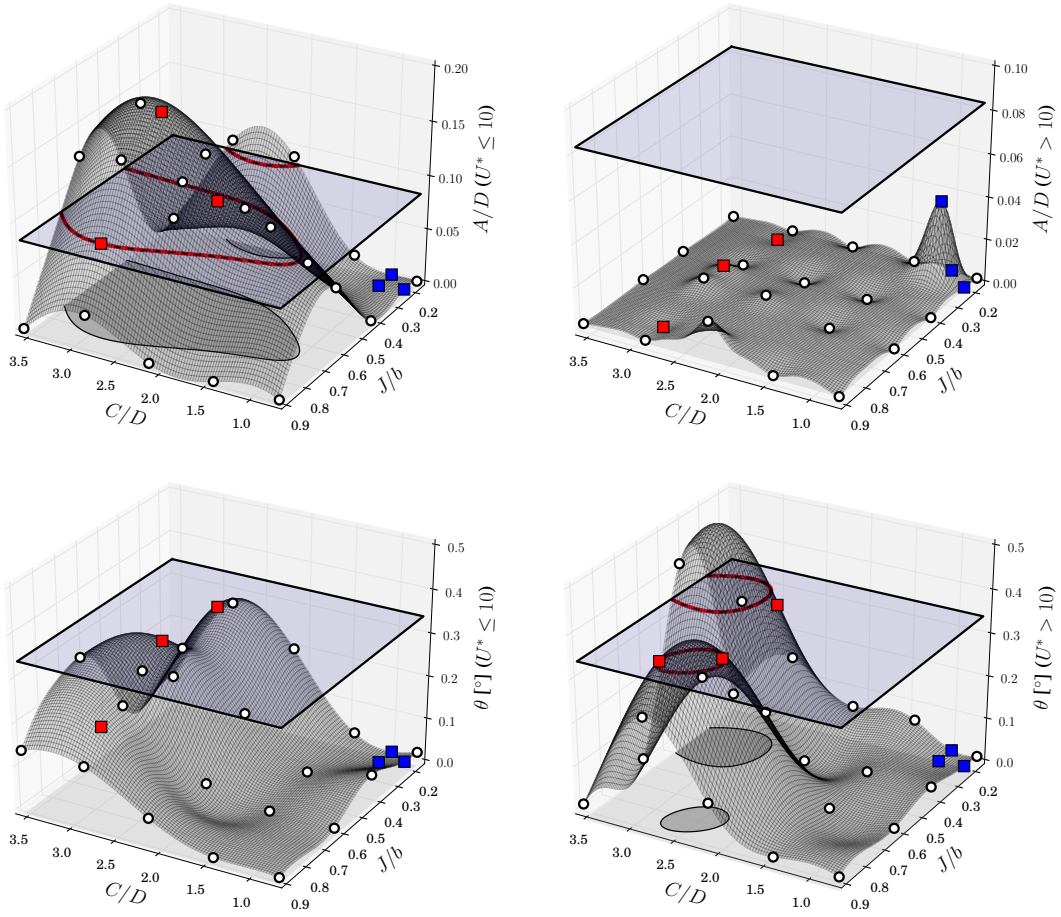

Figure 20: Surrogate model trained with the full set of samples, including the new values reported in Table 6 to increase the accuracy in the neighborhood of the solution. New data shown as blue squares.

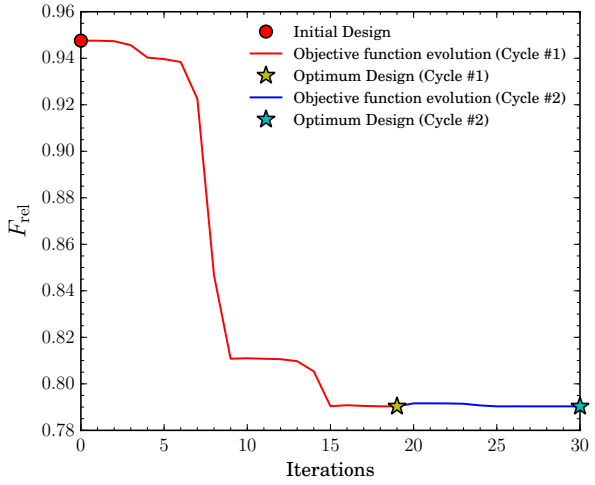

Figure 21: Convergence of the objective function F after completing two optimization cycles.

Table 7: Comparison of the shape design variables $\boldsymbol{S}_d = [C, J]$, objective function expressed in relative values F_{rel}, and VIV responses used as design constraints of the initial design and optimum designs obtained in the two optimization cycles performed.

Design	C/D	J/b	F_{rel} [-]	$\theta\,[^\circ]\,(U^* \leq 10)$	$\theta\,[^\circ]\,(U^* > 10)$	$A/D\,(U^* \leq 10)$	$A/D\,(U^* > 10)$
$\boldsymbol{S}_{d,0}$	2.857	0.424	0.9476	0.2466	0.3549	0.0870	0.0037
$\boldsymbol{S}^*_{d,1}$ (Cycle #1)	0.714	0.181	0.7903	0.0253	0.0215	0.0002	0.0018
$\boldsymbol{S}^*_{d,2}$ (Cycle #2)	0.714	0.162	0.7903	0.0199	0.0110	0.0022	0.0017

shortened from 11.2 m to 2.8 m in full scale, which reduced the deck cost by approximately \$26M (15.7%). The maintenance track was moved from its original location, attached to the bottom plate, to the outer inclined plate. The proposed methodology was able to obtain a less expensive design without the occurrence of VIV in a systematic fashion while dealing with several design variables and constraints simultaneously without relying on heuristic methods based on the engineer's experience. The formulation proposed in Equation (1) is absolutely general. It can be extended by adding more aeroelastic phenomena in the design problem, as it was done in the aero-structural optimization method reported in Cid Montoya et al. [62], where flutter and buffeting responses were simultaneously controlled. Moreover, the formulation can be further generalized by adding more design constraints that limit the VIV and other aeroelastic responses at several angles of attack to guarantee the stability of the deck under different wind conditions.

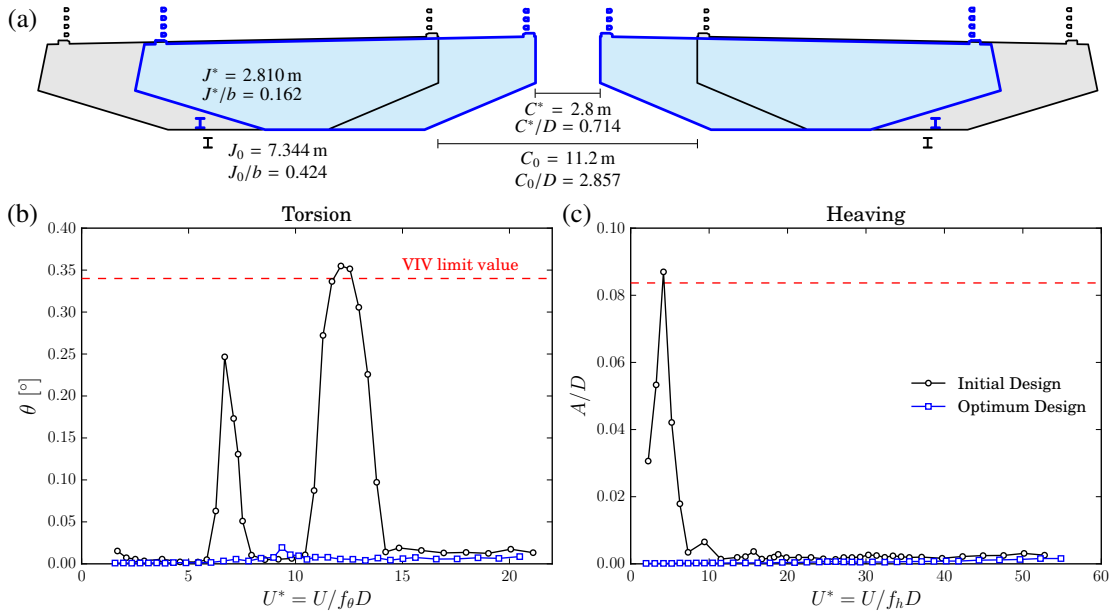

Figure 22: Comparison of the initial (gray) and optimum design (blue): (a) deck cross-section configuration showing the gap distance C and the position of the maintenance track J (dimensions in full scale and non-dimensional values); (b) torsional VIV response; and (c) heaving VIV response.

5. Concluding remarks

This study proposes a wind tunnel data-driven surrogate-based design optimization framework to efficiently address the inherent challenges in the preliminary and final phases of the aerodynamic design of long-span bridge decks. The methodology advances the current heuristic design methods by simultaneously considering all relevant shape design variables in the VIV-resistant design of bridges and by iteratively updating the sampling plan moving from a global to a local focus. This strategy permits an effective and accurate optimization-driven aerodynamic tailoring of decks. Wind tunnel test data is used to build aeroelastic surrogates that allow the optimization algorithm to handle the VIV bridge responses as design constraints. An economic model is used to minimize the cost of the bridge, typically controlled in the case of twin-box decks by the transversal beam cost. A balance between economic short-gap designs and aeroelastic-stable designs is achieved based on the thresholds imposed by the Code of Wind-resistant Design Specification for Highway Bridges (JTG/T 3360-01-2018) of China and the gap-driven natural frequencies. The surrogate-based strategy completed two cycles. The first cycle performed a global sampling over the entire design domain to explore all possible design configurations. A full factorial sampling strategy was adopted to reduce the construction costs of the sectional models and wind tunnel testing workload. This first cycle permitted the identification of regions of the design domain where VIV is not present for either the vertical or torsional degrees of freedom. The presence of disjoint feasible design regions is an expected characteristic of VIV surrogates due to the inherent nonlinear nature of bluff bodies' aerodynamics that justifies the iterative outer loop of the proposed method. The second cycle carried out a local sampling to create a trust region where the optimization algorithm can accurately converge to an optimum design independently of the resolution of the first cycle sampling. All experimental data measured to extract the VIV amplitudes were reported. The optimization algorithm reduced the gap to the minimum thanks to the good VIV performance and the economic benefits of adopting shorter transversal beams. The optimum position for the maintenance rails was found in the outer inclined plates. The proposed optimization methodology effectively mitigated the VIV responses while achieving relevant reductions in the deck cost.

Acknowledgments

Miguel Cid Montoya gratefully acknowledges the support of NSF under grant CMMI #2301824 and the new faculty start-up funds provided by Texas A&M University-Corpus Christi. Hua Bai gratefully acknowledges financial support from the Natural Science Foundation of Shaanxi Province, China, under grant No. 2023-JC-YB-408.

References

[1] Y.-J. Ge. Aerodynamic challenge and limitation in long-span cable-supported bridges. In *The 2016 World Congr. on Advances in Civil, Environ., and Materials Research*, 2016.

[2] A. Larsen and G. Larose. Dynamic wind effects on suspension and cable-stayed bridges. *Journal of Sound and Vibration*, 334:2–28, 2015. doi: 10.1016/j.jsv.2014.06.009.

[3] A. Larsen, S. Esdahl, J. E. Andersen, and T. Vejrum. Storebælt suspension bridge – vortex shedding excitation and mitigation by guide vanes. *J Wing Eng Ind Aerod*, 88:283–296, 2000.

[4] G. Diana, F. Resta, M. Belloli, and D. Rocchi. On the vortex shedding forcing on suspension bridge deck. *Journal of Wind Engineering and Industrial Aerodynamics*, 92(5):341–363, 2006.

[5] W. Zhang, Z. Wei, Y. Yang, and Y. Ge. Comparison and analysis of vortex induced vibration for twin-box bridge sections based on experiments in different reynolds numbers. *Journal of Tongji University (Natural Science)*, 36(1):6–11, 2008.

[6] Y. Yang, J. Zhang, F. Cao, Y. Ge, and L. Zhao. Evaluation and improvement of wind environment and vehicle safety on long-span bridge deck under strong crosswind. *J. Wind Eng. Ind. Aerod.*, (228), 2022.

[7] K. Xu, Y. Ge, and L. Zhao. Quantitative evaluation of empirical models of vortex-induced vibration of bridge decks through sectional model wind tunnel testing. *Engineering Structures*, 219:110860, 2020.

[8] M. A. Astiz. Wind-induced vibrations of the Alconétar Bridge, Spain. *Struct. Eng. Int.*, 20 (2):195–199, 1999.

[9] Y. Ge, L. Zhao, and J. Cao. Case study of vortex-induced vibration and mitigation mechanism for a long-span suspension bridge. *J. Wind Eng. Ind. Aerod.*, (220):104866, 2022.

[10] A. Zasso, T. Argentini, S. Omarini, D. Rocchi, and O. Oiseth. Peculiar aerodynamic advantages and problems of twin-box girder decks for long span crossings. *Bridge Structures*, 15 (3):111–120, 2019.

[11] T. Argentini, D. Rocchi, C. Somaschini, U. Spinelli, F. Zanelli, and A. Larsen. Aeroelastic stability of a twin-box deck: Comparison of different procedures to assess the effect of geometric details. *J Wing Eng Ind Aerod*, 220:104878, 2022.

[12] X. R. Qin, K. C. S. Kwok, C. H. Fok, P. A. Hitchcock, and Y. L. Xu. Wind-induced self-excited vibrations of a twin-deck bridge and the effects of gap-width. *Wind and Structures*, 10(5):463–479, 2007.

[13] K. C. S. Kwok, X. R. Qin, C. H. Fok, and P. A. Hitchcock. Wind-induced pressures around a sectional twin-deck bridge model: Effects of gap-width on the aerodynamic forces and vortex shedding mechanisms. *J. Wind Eng. Ind. Aerodyn.*, 110:50–61, 2012.

[14] Y. Yang, R. Zhou, Y. Ge, S. Mahotti, and P. Mendis. Aerodynamic instability performance of twin box girders for long-span bridges. *J Wing Eng Ind Aerod*, 145:196–208, 2015.

[15] Y. Yang, R. Zhou, Y. Ge, and L. Zhang. Experimental studies on viv performance and countermeasures for twin-box girder bridges with various slot with ratios. *Journal of Fluids and Structures*, 66:476–489, 2016.

[16] C. A. Trein, H. Shirato, and M. Matsumoto. On the effects of the gap on the unsteady pressure characteristics of two-box bridge girders. *Engineering Structures*, 82:121–133, 2015.

[17] F. Nieto, M. Cid Montoya, S. Hernández, I. Kusano, A. Casteleiro, A. J. Álvarez, J. Á. Jurado, and A. Fontán. Aerodynamic and aeroelastic responses of short gap twin-box decks: Box geometry and gap distance dependent surrogate based design. *J Wing Eng Ind Aerod*, 201:104147, 2020.

[18] J. Wang, C. Ma, H. Jing, C. Pei, and E. Dragomirescu. Aerodynamic admittance of streamlined bridge decks. *J. Wind Eng. Ind. Aerodyn.*, 198:104080, 2020.

[19] J. Wang, C. Ma, Q. S. Li, and H. Qin. Influence of gap width on buffeting force spatial correlation and aerodynamic admittance of twin-box bridge deck. *J. Wind Eng. Ind. Aerodyn.*, 207:104392, 2020.

[20] S. Laima and H. Li. Effects of gap width on flow motions around twin-box girders and vortex-induced vibrations. *J. Wind Eng. Ind. Aerodyn.*, 139:37–49, 2015.

[21] A. J. Álvarez, F. Nieto, K. C. S. Kwok, and S.. Hernández. Aerodynamic performance of twin-box decks: A parametric study on gap width effects based on validated 2D URANS simulations. *J. Wind Eng. Ind. Aerodyn.*, 182 (2):202–221, 2018.

[22] ASCE Committee on Cable-Stayed Bridges. *Guidelines for the design of cable-stayed bridges.* 1992. URL `https://ascelibrary.org/doi/book/10.1061/9780872629004`.

[23] JTGT 3360-01-2018. *Wind-resistant design code for highway bridges (JTGT 3360-01-2018) (in Chinese).* 2019.

[24] ISO 2631. Mechanical vibration and shock - Evaluation of human exposure to whole-body vibration. Technical report, ISO, 2018.

[25] Stretto di Messina. Messina Strait Bridge: Basis of design and expected performance (italian: Ponte sullo Stretto di Messina: Fondamenti progettuali e prestazioni attese per l'opera di attraversamento). Technical report, Stretto di Messina Report GCG.F.04.01, 2004.

[26] M. Hosomi, H. Kobayashi, and Y. Nitta. Fatigue strength design for vortex-induced oscillation and buffeting of a bridge. *J. Wind Eng. Ind. Aerod.*, 67-68:227–237, 1997.

[27] M. Gu, S.R. Chen, and C.C. Chang. Control of wind-induced vibrations of long-span bridges by semi-active lever-type tmd. *J. Wind Eng. Ind. Aerod.*, 90(2):111–126, 2002.

[28] R. C. Battista and M. S. Pfeil. Reduction of vortex-induced oscillations of rio–niterói bridge by dynamic control devices. *J Wing Eng Ind Aerod*, 83(3):273–288, 2000.

[29] W. C. Brown. Long span suspensión bridges: A british approach. *Annals of the New York Academie of Sciences*, 352(1):1–26, 1980.

[30] A. Larsen and A. Wall. Shaping of bridge box girders to avoid vortex shedding response. *Journal of Wind Engineering and Industrial Aerodynamics*, 104-106:159–165, 2012.

[31] M. Belloli, F. Fossati, S. Giappino, and S. Muggiasca. Vortex induced vibrations of a bridge deck: Dynamic response and surface pressure distribution. *J. Wind Eng. Ind. Aerod.*, 133: 160–168, 2014.

[32] T. Vejrum, D. J. Queen, G. L. Larose, and A. Larsen. Further aerodynamic studies of lions' gate bridge – 3 lane renovation. *J Wing Eng Ind Aerod*, 88:325–341, 2000.

[33] M. Barelli, J. White, and D. P. Billington. History and aesthetics of the bronx-whitestone bridge. *J. Bridge Eng.*, 11 (2):230–240, 2006.

[34] R. Kargarmoakhar, A. G. Chowdhury, and P. A. Irwin. Reynolds number effects on twin box girder long span bridge aerodynamics. *Wind and Structures*, 20:327–347, 2015.

[35] Y. Nakamura and T. Mizota. Unsteady lifts and wakes of oscillating rectangular prisms. *Journal of Engineering Mechanics Division*, 101:855–871, 1975.

[36] S. Komatsu and H. Kobayashi. Vortex-induced oscillation of bluff cylinders. *Journal of Wind Engineering and Industrial Aerodynamics*, 6(3-4):335–362, 1980.

[37] N. Shiraishi and M. Matsumoto. On the classification of vortex-induced oscillations and its application for bridge structures. *Journal of Wind Engineering and Industrial Aerodynamics*, 14(1-3):419–430, 1983.

[38] H. Bai, R. Li, G. Xu, and A. Kareem. Aerodynamic performance of π-shaped composite deck cable-stayed bridges including VIV mitigation measures. *J Wing Eng Ind Aerod*, 208: 104451, 2021.

[39] M. Li, Y. Sun, H. Jing, and M. Li. Vortex-induced vibration optimization of a wide streamline box girder by wind tunnel test. *KSCE Journal of Civil Engineering*, 22(12):5143–5153, 2018.

[40] R. Zhou, Y. Ge, Q. Liu, Y. Yang, and L. Zhang. Experimental and numerical studies of wind-resistance performance of twin-box bridges with various grid plates. *Thin-Walled Structures*, 166:108088, 2021.

[41] Y. Yang, R. Zhou, Y. Ge, X. Zou, and L. Zhang. Flutter characteristics of twin-box girder bridges with vertical central stabilizers. *Engineering Structures*, (133):33–48, 2017.

[42] H. Bai, N. Ji, G. Xu, and J. Li. An alternative aerodynamic mitigation measure for improving bridge flutter and vortex induced vibration (VIV) stability: Sealed traffic barrier. *J Wing Eng Ind Aerod*, 206:104302, 2020.

[43] D. Gao, Z. Deng, W. Yang, and W. Chen. Review of the excitation mechanics and aerodynamic flow control of vortex-induced vibration of the main girder for long-span bridges: A vortex-dynamics approach. *Journal of Fluids and Structures*, 105:103348, 2021.

[44] C. Wang, X. Hua, Z. Feng, H. Xiao, Z. Chen, and J. Zhang. Experimental investigation on vortex-induced vibrations of a triple-box girder with web modification. *J Wind Eng Ind Aerodyn*, 218:104783, 2021.

[45] Ö. Güzel. Advanced planning and innovative construction technologies in the challenging bridge projects. In *IABSE Symposium Istanbul 2023: Long Span Bridges; Istanbul, Türkiye; 26-28 April 2023*, 2023.

[46] E. Arıoğlu. Importance of "heuristics" in suspension bridge engineering and 1915 Çanakkale bridge. *Springer Tracts on Transportation and Traffic*, 17:19–41, 2021.

[47] L.A. Schmit and W. A. Thornton. Synthesis of an airfoil at supersonic Match number. Technical report, NASA CR-144, 1965.

[48] G. N. Vanderplaats. *Numerical optimization techniques for engineering design.* Vanderplaats Research & Development Inc., Colorado Springs, USA, 2001.

[49] S. R. Hansen and G. N. Vanderplaats. Approximation method for configuration optimization of trusses. *AIAA J*, 28:161–168, 1990.

[50] A. I. J. Forrester and A. J. Keane. Recent advances in surrogate-based optimization. *Progress in Aerospace Sciences*, 45(1-3):50–79, 2009.

[51] N. V. Queipo, R. T. Haftka, W. Shyy, T. Goel, R. Vaidyanathan, and P. K. Tucker. Surrogate-based analysis and optimization. *Prog. Aero. Sci.*, 41(1):1–28, 2005.

[52] R. Yondo, E. Andrés, and E. Valero. A review on design of experiments and surrogate models in aircraft real-time and manu-query aerodynamic analyses. *Prog. Aero. Sci.*, 96: 23–61, 2018.

[53] H. Adeli and S.-L. Hung. *MAchine learning: Neural networks, genetic algorithms, and fuzzy systems.* John Wiley and Sons, 1994.

[54] F. Rizzo and L. Caracoglia. Artificial neural network model to predict the flutter velocity of suspension bridges. *Computers & Structures*, 233:106236, 2020.

[55] G. E. Erten, M. Yavuz, and C. V. Deutsch. Combination of machine learning and kriging for spatial estimation of geological attributes. *Natural Resources Research*, 31:191–213, 2022.

[56] M. Cid Montoya, F. Nieto, S. Hernández, I. Kusano, A. J. Álvarez, and J. Á. Jurado. CFD-based aeroelastic characterization of streamlined bridge deck cross-sections subject to shape modifications using surrogate models. *J Wind Eng Ind Aerod*, 177:405–428, 2018.

[57] G. Xu, A. Kareem, and L. Shen. Surrogate modeling with sequential updating: applications to bridge deck-wave and bridge deck-wind interactions. *ASCE J. Comput. Civ. Eng.*, 34(4): 04020023, 2020.

[58] M. Cid Montoya, S. Hernández, and F. Nieto. Shape optimization of streamlined decks of cable-stayed bridges considering aeroelastic and structural constraints. *J Wind Eng Ind Aerod*, 177:429–455, 2018.

[59] M. Cid Montoya, S. Hernández, and A. Kareem. Aero-structural optimization-based tailoring of bridge deck geometry. *Eng Struct*, 270:114067, 2022.

[60] M. Cid Montoya. Sequential aero-structural optimization method for efficient bridge design. *Computer-Aided Civil and Infrastructure Engineering*, In Press, 2023.

[61] M. Cid Montoya, F. Nieto, S. Hernández, A. Fontán, J. Á. Jurado, and A. Kareem. Aero-structural optimization of streamlined twin-box deck bridges with short gap considering flutter. *J. Bridge Eng.*, 26(6):04021028, 2021.

[62] M. Cid Montoya, F. Nieto, S. Hernández, A. Fontán, J. Á. Jurado, and A. Kareem. Optimization of bridges with short gap streamlined twin-box decks considering structural, flutter and buffeting performance. *J Wing Eng Ind Aerod*, 208:104316, 2021.

[63] G. Diana, D. Rocchi, and M Belloli. Wind tunnel: a fundamental tool for long-span bridge design. *Structure and Infrastructure Engineering*, 11(4):533–555, 2015.

[64] A. Buljac, H. Kozmar, S. Pospisil, and M. Machacek. Aerodynamic and aeroelastic characteristics of typical bridge decks equipped with wind barriers at the windward bridge-deck

edge. *Engineering Structures*, 137:310–322, 2017.

[65] H. Li, X. He, L. Hu, and G. Xu. Quantification of aerodynamic forces for truss bridge-girders based on wind tunnel test and kriging surrogate model. *Advances in Structural Engieering*, 24(10):2161–2175, 2021.

[66] A. Putil, S. Jung, S. Lee, and S.-D. Kwon. Mitigation of vortex-induced vibrations in bridges under conflicting objectives. *J. Wind Eng. Ind. Aerod.*, 99:1243–1252, 2011.

[67] D. G. Krige. A statistical approach to some basic mine valuation problems on the witwatersrand. *Journal of the Chemical, Metallurgical and Mining Engineering Society of South Africa*, 52(6):119–139, 1951.

[68] J. Sacks, W. J. Welch, T. J. Mitchell, and H. Wynn. Design and analysis of computer experiments. *Statistical Science*, 4(4):409–423, 1989.

[69] A. I. J. Forrester, A. Sóbester, and A. J. Keane. *Engineering Design via Surrogate Modelling*. Wiley, July 2008.

[70] M. D. McKay, R. J. Beckman, and W. J. Conover. A comparison of three methods for selecting values of input variables in the analysis of output from a computer code. *Technometrics*, 21(2):239 – 245, 1979.

[71] A. Olsson, G. Sandberg, and O. Dahlblom. On latin hypercube sampling for structural reliability analysis. *Structural Safety*, 25(1):47 – 68, 2003. ISSN 0167-4730. Latin hypercubes;.

[72] V. Picheny, D. Ginsbourger, O. Roustant, R. T. Haftka, and N.-H. Kim. Adaptive designs of experiments for accurate approximation of a target region. *Journal of Mechanical Design, Transactions of the ASME*, 132:0710081–0710089, 2010.

[73] D. C. Montgomery. *Design and Analysis of Experiments*. John Wiley and Sons, Inc., New York, 8^{th} ed., 2012.

[74] P. A. Irwin. Bluff body aerodynamics in wind engineering. *Journal of Wind Engineering and Industrial Aerodynamics*, 96:701–712, 2008.

[75] V. K. Garg and R. V. Dukkipati. *Dynamics of Railway Vehicle Systems*. Academic Press, Canada, Ontario, 1984.

[76] M. Pia Repetto and G. Solari. Directional wind-induced fatigue of slender vertical structures. *J. Struct. Eng.*, 130(7):1032–1040, 2004.

[77] X. Chen. Analysis of crosswind fatigue of wind-excited structures with nonlinear aerodynamic damping. *Engineering Structures*, 74:145–156, 2014.

[78] J. H. Holland. *Adaptation in Natural and Artificial Systems*. University of Michigan Press, 1975.

[79] M. Wahde. *Biologically Inspired Optimization Methods*. WIT Press, 2008.

[80] S. Hernández. Structural optimization. 1960-2010 and beyond. *Comput. Technol. Rev.*, 2: 177, 2010.

[81] H. W. Kuhn and A. W. Tucker. Nonlinear programming. In *Proceedings of 2nd Berkeley Symposium. Berkeley: University of California Press. pp. 481–492.*, 1951.

[82] Raphael T Haftka and Zafer Gürdal. *Elements of structural optimization*. Springer, 1992. ISBN 9780792315049.

[83] J. S. Arora. *Introduction to optimum design*. Elsevier/Academic Press, 3^{th} edition, 2011.

[84] *GENESIS User's Manual, Version 18.0*. Vanderplaats Research and Development, Inc., 2019.

[85] *OptiStruct User's Manual, Version 2021.2*. Altair HyperWorks, 2021.

[86] Vanderplaats Research and Inc. Development. DOT users manual, version 4.20. Technical report, 1995.

[87] *MATLAB and Optimization Toolbox Release 2022a*. The MathWorks, Inc., Natick, Massachusetts, United States, 2022.

[88] W.-L. Chen, H. Li, and H. Hu. An experimental study on the unsteady vortices and turbulent flow structures around twin-box-girder bridge deck models with different gap ratios. *J Wing Eng Ind Aerod*, 132:27–36, 2014.

[89] A. Camera, A. Bagnara, A. Larsen, S. Cammelli, and G. Piccardo. The effect of central gap and wind screens on the aeroelastic stability of long-span bridge decks: Comparison of numerical analyses and experimental results. *Journal of Fluids and Structures*, 121:103923,

2023.

[90] S. Xu, G. Fang, O. Øiseth, L. Zhao, and Y. Ge. Experimental study on distributed aerodynamic forces of parallel box girders with various slot width ratios and aerodynamic countermeasures during vortex-induced vibration. *J Wing Eng Ind Aerod*, 240:105493, 2023.

[91] M. S. Andersen, M. B. Eriksen, S. V. Larsen, and A. Brandt. The influence of gap- and chord-widths for multi-box girders: Superposition of flat plate flutter derivatives and section model tests. *Journal of Fluids and Structures*, 109:103489, 2022.

[92] I. B. Kroon, H. Park, A. Özener, D. Mete, and Y. Yamasaki. 1915 Çanakkale bridge - detailed design. In *IABSE Symposium Istanbul 2023: Long Span Bridges; Istanbul, Türkiye; 26-28 April 2023*, 2023.

[93] H. Sato, S. Kusuhara, K.-I. Ogi, and H. Matsufuji. Aerodynamic characteristics of super long-span bridges with slotted box girder. *J Wing Eng Ind Aerod*, 88:297–306, 2000.

[94] Y. Yang, T. Wu, Y. Ge, and A. Kareem. Aerodynamic stabilization mechanism of a twin box girder with various slot widths. *ASCE J Bridge Eng*, 20(3):04014067, 2015.

[95] F. Nieto, M. Cid Montoya, A. Fontán, S. Hernández, C. Rapela, A. J. Álvarez, J. Á. Jurado, A. Casteleiro, and V. García. Wind tunnel study on the effect of the gap width in the aerodynamic and aeroelastic responses of twin-box decks. In *WIT Transactions on Engineering Sciences, Advances in Fluid Mechanics XII*, volume 120, pages 61–69, 2018.

[96] L. Tophøj and S. O. Hansen. A point vortex model for aerodynamic derivatives for tandem multi-deck structures. *J Wing Eng Ind Aerod*, 188:421–434, 2019.